COGEAR

MODULE 3:

Development of a 3D model of the Matter valley

Del. No.: 3b.2.5

Author: Yugsi, F.

Engineering Geology, ETH Zürich

March 4, 2011

DISS. ETH NO. 19461

STRUCTURAL CONTROL OF MULTI-SCALE DISCONTINUITIES ON SLOPE INSTABILITIES IN CRYSTALLINE ROCK (MATTER VALLEY, SWITZERLAND)

A dissertation submitted to
ETH ZURICH

for the degree of

Doctor of Sciences

presented by

FREDDY XAVIER YUGSI MOLINA
Ingeniero Geólogo, Escuela Politécnica Nacional, Ecuador

born 29.11.1974

citizen of Ecuador

accepted on the recommendation of

Prof. Dr. Simon Loew, examiner
Prof. Dr. Michel Jaboyedoff, co-examiner
Dr. Reginald Hermanns, co-examiner

2010

Chapter 2

Multi-scale rock mass structure from integrated field and high-resolution DEM investigation using Geographic Information Systems (Matter Valley, Switzerland)

2.1 Introduction

2.1.1 Rock Mass Characterization

Geotechnical characterization of rock masses is a common task that has been applied for multiple purposes related with engineering problems such as underground excavations or slope stability assessments. A good knowledge of the internal geometry of a rock mass is essential for the understanding of the behavior when external conditions change or undergo periodical variations (i.e. seasonal changes in environmental conditions). There are several components that can be included to characterize a rock mass and they will depend on the purpose of the characterization. For example, several rock mass characterization systems have been developed to predict rock mass behavior on underground and slope excavation projects. Some of the most popular systems are Q (Barton et al., created on 1974, revised on 1993 and 2002), RMR (Bienawski, created on 1973 revised 1988), and GSI (Hoek, created on 1995, several revisions e.g. Cai et al., 2004). They include mechanical characteristics of the intact rock, physical and geometrical properties of discontinuities and external factors like stress conditions, or groundwater pressure. However, their application requires detailed information of site conditions. This level of detail cannot be achieved on areas of difficult access such as mountainous regions, where characterization of rock masses are carried out involving fewer parameters. The present study is focused on the characterization of the discontinuities (mainly fractures) directed to the assessment of failure potential of crystalline rock slopes. Previous works have shown the importance of fracture properties in the occurrence and development of failures in rock slopes (Brideau et al.., 2009; Brideau et al.., 2006; Mazzoccola & Hudson, 1996; Brady & Brown, 2004). Fractures have an influence on the failure process because they control the kinematics and stability of larger scale rock masses in slopes.

2.1.2 Discontinuities

The term fracture is used for all kinds of effective discontinuities with zero or low tensile strength. Fractures are classified according with their length and type of movement. Faults are brittle shear zones for which visible displacements have occurred, primarily parallel to the fault plane. Joints are fractures in meso-scale dimension for which no shear offset or dilation is detectable in the field. Schistosity is a penetrative rock fabric and a potential discontinuity, defined by a parallel alignment of platy minerals in metamorphic rocks, producing an inter-leaving or foliation structure.

Fractures have been divided for the present work according to their persistence in large scale discontinuities (visible trace length of hectometers, i.e. more than one hundred meters) and meso-scale discontinuities (visible trace length of meters to decameters; i.e. less than one hundred meters and more than 10 centimeters). Whereas most meso-scale discontinuities are joints, large scale discontinuities are brittle and brittle-ductile shear zones (i.e. faults). The term fracture is used in this paper to describe all types of effective discontinuities (breaks in rocks), irrespectively of size or mode of failure.

Discontinuity orientation has been used in the present analysis as the main discontinuity property and intensive data collection using different methods have been carried out. Orientation is defined by the dip of the line of maximum declination on the discontinuity surface measured from the horizontal, and the dip direction or azimuth of this line, measured clockwise from true north (Brady & Brown, 2004).

Large scale discontinuities play an important role in the development of large instabilities in mountainous environments. Usually, boundaries of deep seated slope gravitational deformations are reactivated pre-existent brittle faults (Agliardi et al., 2001; Brideau et al., 2009). In the study area, the 1991 rockslides at Randa had an important structural control as the failed rock mass was segmented in several compartments limited by persistent fractures (Sartori et al., 2003)Moreover, faults control the kinematics of the current instability at Randa (Willenberg et al., 2008; Gischig et al., 2009).

Meso-scale fractures are an important factor that condition smaller scale slope instabilities. For example the rockslope failure of Medji in 2002, was controlled by two meso-scale joint sets (Ladner et al., 2004). Also the current instability at Calchofen is controlled by meso-scale fractures (Rouiller et al., 1998).

2.1.3 Objectives of Study

Mountainous areas are regions considered prone to the occurrence of catastrophic rock slope failure because of their geomorphological characteristics and discontinuity geometry. The latter is considered an important factor on the occurrence of rock slope instabilities. Large instabilities in natural rock slopes have always represented a threatening factor to the development and expansion of human settlements and vital transportation networks. They have caused substantial economical and life losses during historical time. A better understanding of failure mechanisms is especially important for unstable slopes in fractured rock masses, where failure has been postulated to develop progressively by strength degradation, failure of intact rock bridges, and internal rock mass deformation. Factors controlling the long term evolution of failure surfaces in brittle rock slopes may include cyclic pore pressure and temperature variations, chemical weathering, seismic loading, and slope toe erosion. However, the most important factors that make a

slope prone to failure are their structural configuration and geometry, since both together govern the deformability, strength and permeability of any rock mass.

A detailed structural characterization of rock masses is essential for a rock slope stability analysis. For the case of natural rock slopes, because of their accessibility and altitudinal changes, a throughout data collection by traditional field techniques presents several limitations due to spatial coverage and the size of the sampling areas. New techniques for structural characterization of rock masses focused primarily on discontinuity orientation have been developed on recent years. Several of those techniques take advantage of the recent developments on remote sensing data acquisition and digital elevation model generation. New methods such as LIDAR or ground based photogrammetry have greatly contributed to the development of high resolution digital elevation models where new methods for manual and semiautomatic detection of planes representing discontinuities have been created based on vector geometry, e.g. COLTOP (Jaboyedoff & Couture, 2003). Co-planarity principles have been used to delimit discontinuity's trace areas (Lato et al., 2009). Another approach is through the detection of linear objects that represent discontinuities via remote sensing imagery. Orientation extraction of those lineaments is done using vector geometry with the help of digital elevation models in a similar fashion as described on Feng et al. (2001) for the case of linear features surveyed by a non-reflector total station. These works have been focused mainly to specific sites such as open pit mines or selected natural rock slopes. Regional analysis using similar tools are scarce and usually only including one of those considerations.

On the present work, three different approaches for the use of GIS-based tools and DEM analysis on structural characterization of rock masses are presented. They were developed based on the criteria mentioned above. Their results were integrated and compared with the results from field work. Commercial software (ArcGIS) has been used for the analysis. GIS have shown to be powerful tools which help to integrate and simultaneously analyze several sources and types of information in a user friendly environment. The area selected for the analysis corresponds to the western flank of the Matter Valley in the southern Swiss Alps. The area presents exceptional conditions for the application and validation of the methodologies presented on this work (e.g. abundant rock faces controlled by rock discontinuities, scarce or inexistent vegetation covering rock outcrops). Additionally, the area presents intense rockfall activity represented on large debris cones deposits to the bottom of rock walls (Figure 2.1). Further descriptions of the study area are presented bellow.

A detailed and systematic structural characterization for the study area (Figure 2.1) does not exist. Detail fracture characterizations have been done for few small areas, which were affected by past failures (Joerg, 2008; Willenberg, 2004) or in small areas with high failure potential (Wagner, 1991). The results from these local investigations are summarized in Chapter 4. For the present work intensive field data collection was carried out in order to derive a comprehensive description of the large and meso-scale discontinuity inventory for the whole study area. New GIS-based remote sensing methodologies were developed to complement the field data sets.

2.2 Geomorphological and geological setting of study area

2.2.1 Geology and Geomorphology

The study area corresponds to the western flank of the Matter Valley between the localities of Randa and St. Niklaus in the southern Swiss Alps (Figure 2.1). The Matter Valley is a long north-south trending valley of the Matter Vispa in the Swiss Alps and drains into the Rhône Valley. The study area is composed of 11 slope faces between secondary creeks draining to the Matter Vispa, from north to south: Grossgufer, Hohebalme, Guggini, Seemate, Saenggini, Walkerschmatt, Medji, Riedji, Chalchofen, Saelli and Sparru (Figure 2.1).

The area is located in the Penninic Siviez Mischabel nappe which is a tectonic subdivision of the Grand St. Bernard nappe (Escher, 1998; Sartori et al., 2006). The Siviez Mischabel nappe is considered as a recumbent fold more than 40 km width (Genier, 2008) emplaced at 41-36 Ma during the Alpine orogeny (Markley, 1998). It comprises basement rocks that are unconformably overlain by units of greenschist facies rocks, which share the same Tertiary Alpine thermal and kinematic history (Markley, 1999). Basement units comprise gneiss, schist, and amphibolite deformed and metamorphosed to amphibolite facies during the Hercynian orogeny that are intruded by a porphyritic alkaline to subalkaline granite of early Permian age (Thélin, 1987), called the Randa orthogneiss. Cover sequences are formed by a metamorphosed Permo-Carboniferous graphitic mica-schist unit at the base, followed by a thick sequence of Triassic quartzites and green schists (metasedimentary rocks), and at the top, a Triassic dolomite and limestone sequence (Markley, 1999).

The Randa orthogneiss is derived from a subalkaline porphyritic granite (Bussy et al., 1996). In the Matter Valley it reaches its maximum thickness of approximately 1000 m (Sartori et al., 2006) and covers most of the study area. It is mainly porphyritic with K-feldspar phenocrysts (Genier, 2008), but can display several other facies: microgranitic border facies, apophyses and leucocratic aplites, schlieren, and mafic and xenolithic enclaves. Decametric zones of dark quartz-porphyries are also found. In the Matter Valley at least three bands of leucocratic and porphyritic metagranitoids interlaced with the cover units have been observed and considered to be related to the Randa orthogneiss (Genier, 2008). Which present a strong alpine foliation and two lineations. The study area has a main direction of foliation dipping towards the S and SW, which varies in azimuth and dip with height (Zueger, 2007).

The valley has been molded primarily by the action of glaciers. During the last glacial maximum (LGM) which occurred 18000 to 20000 yr BP (Kelly, 2004) the Matter Valley was part of the main accumulation area in the Swiss Alps with a decreasing ice thickness towards the Rhône valley. In the area of Zermatt, the icefield reached an elevation of 3010 masl. In the Matter valley, the ice elevation ranged between 2550-2700 m, 1300 m above its bottom at Randa (Willenberg, 2004). Ice flowed towards north from a central accumulation region at Zermatt. However, not clear evidences such as trimlines were developed into the valley because the variable bedrock lithologies (Kelly, 2004). Glacial release after melting has been estimated to occur around 10000 yr BP (Winistorfer 1977).

Glacial erosion has conditioned the current morphology of the Matter valley. On the western side, front rockwalls parallel to the valley axis, have high dip angles built by glacial erosion and associated paraglacial processes. The steep slopes overprint the original U-shaped valley and are remolded by postglacial erosional and depositional features (Willenberg, 2004). The eastern side slopes of the valley are moderately inclined, and usually foliation-parallel. They are covered with glacial deposits, debris and rockslide material (Schindler & Eisenlohr 1992).

The nature of the response of glacially steepened rock slopes to deglaciation is strongly conditioned by lithology and structure, and in particular, by joint density, and the orientation and inclination of discontinuities and planes of weakness (e.g. foliation, bedding) relative to the rock face (Augustinus, 1995 in Ballantyne, 2002). Augustinus, 1992, demonstrated that steep massive crystalline rock slopes remained stable, with no evidence for deep seated slope failure following glacier retreat. Thus the nature, scale and timing of paraglacial rock adjustment is strongly conditioned by rock mass strength and joint network, being observed that some deep seated failures may occur centuries or millennia after deglaciation (Ballantyne, 2002). In the study area, the influence of these conditions has been expressed by various kinds and magnitudes of past and ongoing rock slope instabilities, which will be summarized in the subsequent sections.

2.2.2 Recent slope instabilities

The rockslide in the western slope close to Randa (Figure 2.2) occurred in 2 different stages in April and May 1991 mobilizing a volume of approximately 30 million of cubic meters. These events destructed the main road and rail line along the valley and dammed the Vispa River that resulted in flooding the town of Randa (Eberhardt *et al.*, 2004). These events have been extensively described in the literature (Wagner 1991, Schindler *et al.*, 1993, Schindler & Eisenlohr 1992, Sartori *et al.*, 2003). Several authors have tried to explain the kinematics and failure process applying diverse techniques based either on 2D numerical simulations (Segalini & Giani 2004, Eberhardt *et al.*, 2004) or 3-D geometrical models representing the sequential release of unstable blocks controlled by the mapped discontinuity geometry (Sartori *et al.*, 2003). The hypothesized causes and mechanisms of these two rockslides include glacial valley erosion and stress accumulation, the destruction of rock bridges between pre-existing fractures, water infiltration and chemical weathering leading to a progressive development of stepped failure surfaces. The progressive failure process was visible in several precursory events within the orthogneiss rock face, such as increasing rock fall activity in the 20 years prior to failure (Schindler *et al.* 1993; Sartori *et al.*, 2003).

Currently, there is a third creeping mass moving towards the valley, located at an altitude between 2000 and 2400 m.a.s.l. at the crown of the two previous slides, having a volume of 3 – 9 million of cubic meters (Loew *et al., 2007*). This creeping mass has been mapped and monitored since the 1991 rockslope failures in great detail. Within the framework of a large SNF funded project, 3 research boreholes were drilled into the unstable rock mass and instrumented with inclinometers, extensometers, pore pressure transducers, and geophones (Willenberg et al. 2008). The instrumentation has been enlarged through the time, including local geodetic networks, climate monitoring, dynamic instrumentations of active fractures,

and investigations of the inaccessible parts of the 1991 failure surfaces with remote sensing techniques such as ground-based differential interferometric radar (Gischig *et al.*, 2009; Moore *et al.* 2010).

These mapping and monitoring campaigns have led to the development of a unique and comprehensive structural and mechanical model of the current instability (Loew, 2007; Gischig *et al.*, 2009) and an in-depth understanding of the mechanisms driving the current slope movements.

The rockslide of Medji (Figure 2.3), a slope to the west of Sankt Niklaus has not been studied as extensively as Randa. However, a good description of the event is given in Ladner *et al.* (2004). The rockslide occurred in November 2002 and involved 120'000 cubic meters of orthogneiss. The slide has a complex surface of rupture consisting of a series of interconnected en echelon fractures that followed the orientation of the main discontinuity sets in the area. Rain and snow melting, were considered as the triggering factors. Chemical weathering caused strength degradation and favored the process initiation. A protection dam built few weeks before the main event reduced drastically the posterior damage caused by the falling rocks. Before the major event, a monitoring network was installed composed of crackmeters, tiltmeters, inclinometers, piezometers and a geodetic monitoring network. Through the interpretation of ground-based radar interferometry and continuous geodetical monitoring, ongoing movement above the area of the 2002 failure has been detected. The current instability is bounded by pre-existent structures (Gischig et al., 2009).

2.3 Foliation and topographic conformity

2.3.1 Spatial variation of schistosity orientation

For the study area, penetrative structures are represented by foliation. According to Milnes et al. (2006), foliation is a general term for a planar arrangement of small-scale textural, crystallographic and/or structural features in any type of rock. In the case of the Matter Valley, foliation corresponds to schistosity on ortho- and para-gneisses. Foliation can cause significant anisotropy in the deformability and strength of rock masses (Priest, 1993). In the western flank of the Matter Valley the schistosity persistently dips gently to the south-west however slight changes in orientation exist. An important fracture sets has developed parallel to this schistosity, making it a key feature for the predisposition of rock failures. Because of that, intensive field work was carried out in the area to evaluate the spatial variation of its orientation. 765 orientations were collected in the field, trying to cover equally the entire study area (Figure 2.4). With this data set, the area was divided in five domains by visual inspection according with the variations of the orientation values. As shown in Figure 2.4, the southern part of the area until the Blattbach River has two clear domains topographically distributed. The upper area of the slopes, above the first slope shoulder, has a clear south-western direction of dip, whereas the lower part close to the bottom valley, clearly dips towards the south. From the Blattbach River to Medji, the dip direction of foliation becomes regular along the full length of the slopes with a general orientation to the south-west. The rest of the area (Sparru) presents a mean dip direction to the west but with a higher scattering than the other areas. This part of

the area has been divided in two different domains because of a clear change in the dip angle values. The dip in the lower part ranges from 15 to 25 while dip angle in the upper part reach values up to 36 degrees (the maximum value for the whole area). Data from all domains are plotted in lower hemisphere, equal angle stereographic projections from which the main orientation of each domain was calculated (Table 2.1).

Kriging techniques were used to create continuous surfaces to estimate the variation of the orientation of foliation within the study area. Field data was used as input. Two separate grids were created for dip and dip direction and evaluated together (Figure 2.5). Kriging is frequently used to spatially interpolate point measurements in numerous Earth system science applications such as mining or soil physics. Kriged estimates are determined with an inverse distance-weighted average of the known z values from a surrounding set of sampling points (Meentemeyer & Moody, 2000). The kriging weights are derived from a semi-variogram that describes the spatial distributions of the sampled values. A special type of kriging called disjunctive kriging was chosen for the present work because it is a good estimator, most of the times better than linear kriging methods (e.g. ordinary, universal kriging). It reduces kriging variance and exactness of estimation even over anisotropic samples (Yates & Warrick, 1986). On disjunctive kriging, data are transformed to normal distributions, which produce stationary bivariate normal distributions for all pairs of data. Conditional probabilities that the true values exceed or are less than a specified critical threshold can then be calculated (Webster & Oliver, 1989). Kriging for dip and dip direction was executed using Geographic Information Systems (GIS). The prediction errors for both parameters are showed in Table 2.2.

2.3.2 Foliation parallel fractures

In the study area, a meso-scale fracture set parallel to the foliation has been identified. In fact, most of the orientations for foliation collected during field work correspond to fractures parallel to foliation. The development of a discontinuity set parallel to pre-existing foliation planes have been observed by many authors (e.g. Milnes et al., 2006; Palmström and Singh, 2001). Usually, foliation and fracture sets are not genetically related but because of the mechanical anisotropy caused by the foliation, fractures follow the planar fabric of the intact rock (Milnes, 2006). In the area this fracture set is persistent but its geometrical characteristics vary greatly. Spacing of this set along the area does not follow a clear spatial variation ranging from few centimeters to few meters. Persistence was observed to follow the trend as in the area of Randa i.e.: around 1 m as the mean value (Willenberg, 2004).

In the study area brittle-ductile shear zones are preferentially following the same orientation as foliation. They were reported to occur in the area of Randa (Willenberg, 2004). Their thickness ranges from few centimeters to several tens of decimeters. They are characterized by a thick band of mylonite-phylonite caused by shearing, highly weathered, which has caused higher rates of erosion. It could imply water circulation into the fracture. Within the shear zone a second steeper foliation is sometimes observable. As it is mentioned in Willenberg (2004), shear zones are bounded by brittle fractures that show slickensides. Persistence can be higher than 100 m. Brittle fractures are associated to Riedel structures.

Domain	Number of measurements	Mean Orientation	
		Dip	Dip Direction
1	67	25	286
2	81	17	272
3	130	16	237
4	193	14	236
5	280	15	207

Table 2.1. Mean orientation values for foliation domains based on field data

2.3.3 Conformity between schistosity and topography

In the area, front walls of the rock slopes are parallel to the trend of the valley axis steeply dipping to the E. For that condition, foliation (schistosity) dip into the slope. In the case of the lateral valleys, side walls have slope angles that dip preferentially N, S, NW and SW. With these conditions, foliation can dip out of the slope in some areas. Several slope-foliation configurations can be critical in terms of slope stability and it becomes important to determine areas with critical slope stability conditions. In order to assess the potential that foliation and foliation-related discontinuities have to create instability of the rock slopes in the area, a classification presented by Powell (1875) has been used. Powell (1875) introduced a classification that represents the conformity between topography and penetrative discontinuities which have been extensively used in the literature (Sander, 1970; Cruden, 1989 in Meentemeyer & Moody, 2000). Slopes are classified into three main classes: cataclinal slopes (slope dips in same direction as discontinuity), anaclinal slopes (slope dips in opposite direction to discontinuity) and orthoclinal slopes (azimuth of slope is perpendicular to azimuth of discontinuity). Cataclinal slopes are subdivided into overdip (slope dip gentler than discontinuity dip), underdip (slope dip steeper than discontinuity dip) and dip (slope dip similar to discontinuity dip). Anaclinal slopes are further divided in normal escarpment (slope dip is perpendicular to discontinuity dip), steepened escarpment (slope dip higher and opposite than discontinuity dip) and subdued escarpment (slope dip lower and opposite than discontinuity dip). Meentemeyer & Moody (2000) proposed a topographic/bedding-plane intersection angle index (TOBIA) to classify natural slopes into the referred classes (Figure 2.6). The system is based on the chord length (L) subtended by the angle between the dip angle of foliation (α) and the dip angle of the slope (A) on the unit circle. Mathematically expressed as:

$$L=\sqrt{(\cos\alpha-\cos A)^2+(\sin\alpha-\sin A)^2} \quad (1)$$

Where:

If $0 \leq L \leq 0.7654$ slope is cataclinal

If $0.7654 < L \leq 1.8748$ slope is orthoclinal

If $1.8478 < L \leq 2$ slope is anaclinal

Subclasses are defined from the dip direction angle of foliation (θ) and the aspect of the slope (S). Thus:

	Cataclinal	**Anaclinal**
If $-5^\circ \leq \theta - S \leq 5^\circ$	Dip slope.	Normal escarpment
If $\theta - S > 5^\circ$ `	Underdip slope.	Subdued escarpment
If $\theta - S < -5^\circ$	Overdip slope.	Steepened escarpment

Prediction errors	**Dip direction**	**Dip**
Mean	0.1451	0.04363
Root mean square	23.84	6.068
Average standard error	22.3	5.628
Mean standardized	0.006635	0.007762
Root mean square standardized	1.069	1.078

Table 2.2. Values of prediction errors for the interpolated surfaces corresponding to dip and dip direction values using disjunctive kriging.

TOBIA was calculated for the study area using the grids created for dip and dip direction of the foliation and the slope and aspect grids derived from a high resolution digital elevation model (DEM). Topographic parameters were extracted from a 2.5m (DEM) created by the assemblage of a 2.5m DEM created by digital photogrammetry techniques with a set of aerial photographs acquired in 2005 and a 2m LIDAR airborne-based DEM provided by SWISSTOPO. The DEMs were merged into a common terrain model as point cloud shapefiles in ArcGiS and a new grid surface was interpolated using natural neighbors. The LIDAR model was preferred for forested steep areas because it has a higher accuracy in such type of terrains. Additionally LIDAR allows vegetation removal. For areas above 2000 m asl, the photogrammetric model was used. Areas above 2000 m asl contain few or none vegetation reducing its influence on the accuracy of the overall model.

As it can be seen in Table 2.3 and Figure 2.7, slopes in the area are predominantly orthoclinal (48. 76%) and anaclinal (47.03%), being the subclass steepened escarpment the most common (44.31%). Together they occupy more than 95% of the area. Orthoclinal slopes are facing mainly to SE and S (Table 2.4), but have an important percentage of slopes dipping to the N, NE and E (38% of their total). Orthoclinal slopes have dip angles varying mainly between 30° and 60°. In a similar way as slope dip direction, orthoclinal slopes have a high scattering for dip angle varying from gentle slopes (<20°) to very steep slopes (>70°). Orthoclinal slopes are evenly distributed along the area with no observable changes.

Steepened escarpments dip preferentially to the E (41.5% of their total). There are no steepened escarpment slopes dipping to SW, W and NW. They have a high slope dip scattering varying mainly from 30° to 70°. There are no slopes dipping less than 10°. Steepened slopes are evenly distributed along the area. To the south of the area they are mainly located in the upper parts of the slope (above 2000 m asl) or in the southern flank of the secondary streams.

Conformity Slope angle	Orthoclinal	Dip Slope	Underdip Slope	Overdip Slope	Normal Escarpment	Subdued Escarpment	Steepened Escarpment	TOTAL
0° - 10°	0.2446	0.0003	0.1014	-	0.0022	0.1745	-	0.5231
10° - 20°	1.0459	0.1264	0.1121	0.0007	0.6768	0.2699	0.0042	2.2361
20° - 30°	4.3676	0.0928	0.0361	0.2536	1.1695	0.0658	2.6954	8.6808
30° - 40°	12.9803	0.0062	0.0004	1.1117	0.3652	0.0009	13.0279	27.4926
40° - 50°	12.5585	-	-	1.0987	0.0001	-	12-3329	25.9901
50° - 60°	8.3625	-	-	0.5672	-	-	8.6167	17.5464
60° - 70°	5.5281	-	-	0.3804	-	-	5.4822	11.3908
70° - 80°	2.9946	-	-	0.2414	-	-	1.9790	5.2150
80° - 90°	0.6790	-	-	0.0757	-	-	0.1703	0.9250
TOTAL	48.7612	0.2257	0.2500	3.7924	2.2139	0.5111	44.3086	100

Table 2.3. Classification of conformity between foliation and slope orientation according to slope angle.

Overdip slopes are not as common as the other two classes but they represent an important issue in terms of stability because dip foliation is gentler than slope dip (can cause planar sliding along the foliation parallel fractures). They occupy around 3.8% of the area and are consistently dipping to the S-SW (95% of their total). They dip preferentially with angles between 30° and 50°. Overdip slopes are not uniformly distributed in the area. They occur more often to the southern part of the area and their occurrence decrease to the north being rare for slopes to the North of Walkerschmatt (Figure 2.7). Overdip slopes are basically located in the lower part of slopes (mainly below 2000 m asl) and are usually forming

part of the northern flanks of secondary streams (which usually cross the area from W to E). The other classes have small representativeness in the area.

2.4 Previous regional fracture investigations

2.4.1 St. Niklaus

Roullier et al. (1998) for the area of Chalchofen, reported 3 main discontinuity sets (Table 2.5) and one main subset with a mean persistence bigger than 50 m and spacing in the order of tens of meters: J1 (024/80), J3 (020/50), J4 (110/50) and J4' (110/70). No further descriptions are presented.

Rovina (unpublished work, 2005) presented a total of four fracture sets for the area of the 2002 Medji rockslide (Table 2.6). Set K1 (025/75) is orientated perpendicular to the valley axis and set K2 (110/80) is orientated parallel to the valley axis. Together these sets are responsible of several pillar-like potential failure masses. The other two sets are less representative but still important: K3 (025/50) and K4 (190/70).

Joerg (2008) described in the area surrounding the rockslide of Medji 2 sets of large scale fractures zones (Table 2.5). The first set (ST1), striking NW – SE, dipping steeply (almost vertical) and a second set (ST2), with a mean orientation of 014/76 and thickness ranging from 15 cm to 30 cm, filled with cataclasite. Faults corresponding to these sets were postulated as the ones that control the 2002 Medji rockslide.

Joerg (2008) described two meso-scale fracture sets (Table 2.6), which were reported as joints: K1 and K2. K1 is described as a set striking to NW-SE (mean orientation 037/77), parallel to a large scale fracture set (ST2). K1 is very persistent with a length in the order of up to tens of meters and spacing intervals from 6 to 20 m. Fractures can be open until 1 m. K2 strikes E – W (mean orientation 096/86), parallel to the valley axis. Persistence can be up to several tens of meters and spacing varies from 1 to 6 m, decreasing to less than 1 m in areas of poor rock mass quality. Quartz and Chlorite have been observed are common fillings for this fracture set. Open fractures can have apertures up to 70 cm.

2.4.2 Herbriggen

Zueger (2007), for the area located between the localities of Randa and Herbriggen, described 5 large scale fracture sets (Table 2.5) with persistence of more than 100 m. Set 1 (192/25) is a set formed by shear zones sub parallel to foliation. Set 2 (076/74) presents often slickensides. It is parallel to the valley axis. Set 3 (012/42) is reported as a ductile shear zone set but it is probably a fault set filled by gouge. Set 4 (021/90 – 201/90) corresponds to a sub vertical fracture zone set that can either dip to the NE or the SW. It is not as frequent as the other three sets. Set 5 (034/69), is described as similar to set 4.

Besides large fracture sets, Zueger (2007) identified 5 sets of meso-scale fractures (Table 2.6). A first set, parallel to foliation, with a mean orientation of 224/14. Other characteristics of the set are persistence 2 m to 10 m, spacing 0.5 m to 1.5 m, planar and closed fractures. A second important set has a mean orientation of 073/70 (parallel to the Matter Valley axis). It was observed that these fractures often present slickensides (162/21). Persistence 1 m to 2 m (up to 10 m), spacing 0.2 m to 3 m, aperture 0.1 cm to 1 cm.

Other sets are reported to be less important for the area. Set 3 (028/77), persistence 1m to 2 m (maximum of 10 m in fracture zones), aperture 0.1 cm to 1 cm. Set 4 (110/80) is not well defined for the whole area, persistence 1 m to 2 m, spacing 1 m to 3 m, aperture less than 0.5 m. Set 5 (348/88), highly scattered, persistence 1 m to 2 m, spacing in the order of several meters, aperture 0.1 cm to 1 cm.

Conformity Slope aspect	Orthoclinal	Dip Slope	Underdip Slope	Overdip Slope	Normal Escarpment	Subdued Escarpment	Steepened Escarpment	TOTAL
North	6.1142	0.0014	0.0012	0.0021	0.0850	0.0245	3.0647	9.2930
North - East	4.9673	-	-	-	0.0834	0.0242	3.0376	7.1815
East	7.6618	-	-	-	1.0148	0.2396	18.3641	27.2802
South - East	16.3330	0.0025	-	0.0226	0.4271	0.0884	5.4806	22.3542
South	12.1258	0.0675	0.0282	2.2594	0.0150	0.0018	0.0719	14.5697
South - West	0.8429	0.1127	0.0875	1.3455	-	-	-	2.3886
West	0.0350	0.0299	0.0530	0.0801	-	-	-	0.1979
North - West	0.6813	0.0118	0.0802	0.0197	-	-	-	0.7929

Table 2.4. Classification of conformity between foliation and slope orientation according to slope aspect.

2.4.3 Randa

Girod (1999) established a different classification of the fracture sets based on the mineralogical origin of fillings and tectonic history (Tables 2.5 and 2.6). His genetic classes are based on observations in the Matter Vispa by-pass tunnel at Randa. He describes five classes of discontinuities. The first class (D1) corresponds to the shear zones parallel to the foliation with high concentrations of calcite, quartz and chlorite. Usually mylonitic layers are related to ductile shearing. The second class (D2) is related to extensional fractures with persistence in the order of meters and tens of meters and variable orientation (062/70, 135/55, 050/60, 080/40) than can correspond to two sets of conjugated fractures. Class D2 presents fillings of quartz and pyrite and in some cases slickensides. Class three (D3) corresponds to hybrid fractures (shear plus extension) with orientations of 070-080/70, fillings of chlorite, persistence smaller than other sets (5 m). Small en echelon tension fractures are associated to this genetic class, which have been reactivated by shearing close to the area of the Randa rockslide. Joints are grouped in a single class (D4). Acording with Girod, joints are defined as smooth planes with absence of fillings associated to fragile elastic deformation. The class is described as variable in orientation, planar and without fillings. A fifth class (D5) is assigned to faults with fillings (gouge) with thickness varying from few centimeters to few decimeters and trace lengths up to several hundred meters. According with the gouge thickness of the fault, they have been classified in thick fillings (031/55), thick to fine fillings (026/90) and fine fillings (010-040/25-60 and 340-350/40-60).

Sartori et al. (2003) reported several sets of "persistent fractures" (Table 2.5) obtained from photo-interpretation of images acquired before, during and after the 1991 rockslides. A differentiation between large and meso-scale fractures is not defined, however, all sets are characterized as persistent which may imply they correspond to large scale fractures. Three main steep orthogonal sets (J2: 060/80, J5: 075/70, J6: 140/80) were found. A single fracture from set 6 (170/80) was reported as the northern limit of the 1991 events. Two less steep fractures (J3: 030/30 and J4: 125/45) were as well reported, being a fracture from J3 set the lower bound of the instable mass that caused the catastrophic events in 1991.

Segalini and Giani (2004) presented four main sets of discontinuities (out of ten) from a structural analysis carried out by Wagner (1991) at Grossgufer (The crown of the May 1991 slope failure at Randa). It is not reported if they correspond to large or meso-scale structures. Two sets (070/66, 160/85) are sub-parallel to the slope and dipping out of the slope with higher angle. Another set (320/35) dips into the slope with a similar angle as the other 2 sets. Finally, a last set (112/46) dipping out of the slope with gentler angle was reported has having a significant importance in the development of the sliding plane for the 1991 rockslide events.

Author	Set 1	Set 2	Set 3	Set 4	Set 5	Set 6
Rouiller	**J3**:020/50	**J1**:024/80		**J4**:110/50		
Girod	**D5**:020-40/90	**D5:**030-040/50	**D3**: 070/70-80			
Sartori			**J2**: 060/80 **J5**: 075/70	**J4**:125/45	**J6**:140/80 **J6'**:170/80	
Willenberg		**F3**:335/41	**F3**:088/65			
Zueger	**S4:**021/90	**S3**:012/42	**S2**:076/74			**S5:**034/69
Joerg	**St1:**195/80	**St2**:014/76				

Table 2.5. Large scale discontinuity sets proposed by other authors for the western flank of the Matter Valley.

Willenberg et al. (2008) for the area of Grossgufer and the slopes above it, determined 3 large scale fracture sets (Table 2.5) and 8 meso-scale fracture sets (Table 2.6). Large and small scale discontinuities were defined differently than in the present work. Small scale fractures are those whose lengths are in the order of decimeter-centimeter whereas large fractures are the ones whose lengths are larger than ten meters. Based on lithology and topographic elevation along the Randa slope, a division of the area in three structural compartments was carried out. 5 meso-scale fracture sets are steep fractures appearing in all structural compartments, with the exception of one of them (set 4), which is absent in compartment I (the area of the 1991 rockslide crown). Set 1 dips to the NE and is normal to foliation. Sets 2-5 include tectonic and stress release fractures with highly scattered orientations, what is related to the changes in lithology, folding, faulting and complex stress release conditions in a complex 3D topography. The remaining three sets (6-8) of Willenberg et al. (2008) have moderate dip angles and are not present in all structural compartments. Set 6 appears in compartments II and III (above the current instability). Sets 7 and 8 appear in compartment I (current instability).

For the large scale fractures, Willenberg described all sets as faults and fracture zones. Fractures from set F-1 are brittle–ductile shear zones parallel to foliation. F-2 set corresponds to brittle faults, brittle–

ductile shear zones and fracture zones dipping N and NW. The NW-dipping major fractures/faults are densely foliated. The F-3 corresponds to faults and fracture zones that strike N–S, parallel to the valley.

2.5 Geometric Properties of Meso-scale Fractures

2.5.1 Field Investigations

For the meso-scale discontinuities in the study area more than 2110 orientations were measured during field recognition. Lineal and spot mapping were used for data collection following the principles presented by Brady & Brown (2004). For lineal mapping a total of 6 scanlines located in the northern part of the area (N of the Blattbach River) were surveyed with a total of 363 measurements. Besides, data collected by Zueger (2007) was included in the analysis for the southern part of the area (a total of 11 scanlines, 490 additional orientations). 990 orientations were collected from spot mapping. Location of spots and scanlines can be seen in Figure 2.8. No subsurface information was available for this work. Despite the extensive field recognition, wide regions of difficult access were not surveyed. The data was plotted on stereonets (equal area, lower hemisphere) and clustered using Fisher distributions (Figure 2.9). Data related with the set of fractures parallel to foliation was not included in the analysis and it is not present in the spot mapping stereplots. Fisher distribution is a symmetrical spherical distribution widely used for stereographical analysis in structural geology. The area was divided in two different domains according with changes in properties observed during the field recognition. The limit between domains is the Blattbach River (Figure 2.1). Four persistent sets not parallel to foliation were observed in the whole area. They show differences in their characteristics between the southern and northern domains.

Author	Set 1	Set 2	Set 3	Set 4	Set 5	Set 6	Others
Girod	**D2:**050-060/60-70	**D2**:135/55					
Rovina			**K1:**025/75	**K2:**110/80	**K4:**190/70		**K3**:025/50
Willenberg	**1**:068/068	**4**:158/77			**3**:229/75	**2**:358/70	**6**:064/39 **7**:302/46 **8**:209/29
Zueger	**S2**:073/70		**S3**:028/77	**S4**:110/80		**S5**:348/88	
Joerg			**K1**:037/77	**K2**:096/86			

Table 2.6: Meso-scale discontinuity sets proposed by other authors for the western flank of the Matter Valley

Set 1 (J1, Table 2.10 Figure 2.9) dips to the SE with a large scattering on its dip direction (circa 50 degrees of variation) and a steep to sub-vertical slope angle (larger than 60 degrees). Set 1 has a trace length ranging in the order of decimeters to meters in the southern domain, increasing substantially to the N where fractures corresponding to this set have lengths in the order of several ten of meters (Figure 2.10). To the N, frequency increases causing the creation of slabs parallel to valley axis (Figure 2.10b). Some of the

fractures present fillings composed of quartz and calcite with slickensides. Fractures are usually closed or with small apertures (< 2 cm). In the northern domain, aperture increases towards the slope face, especially in areas of high relief where it can reach values in the order of tens of centimeters (Figure 2.10). It is the most frequent set in the northern domain (Fisher concentration about 5%).

Set 2 (J2, Table 2.10, Figure 2.9) dips to the E-NE with a steep angle (larger than 60 degrees). Its length varies from decimeters to meters. It is the most frequent set in the southern domain (Fisher concentration about 6.5%). To the N, its frequency and length notably decrease (Fisher concentration about 2%). Fractures can present chlorite fillings. J2 has been reported by all authors that have worked in the southern domain (Girod, 1999; Willenberg , 2004; Zueger, 2007). However, no references exist for this set in the northern domain showing its low rate of occurrence. Its high frequency in the South of the study area can be explained because it corresponds to 2 parallel sets with different origin. A first set of tectonic origin which present slickensides and chlorite infillings and a second set caused by glacier-retreat related processes (exfoliation joints) which is more densely distributed to the S of the Blattbach River. To the N of the Blattbach River the mean orientation of the front face of the slopes rotates about 15° clockwise. This change in the slope orientation produces a decreasing in the frequency of J2 as it can be observed from the stereographic analysis. To the north of the Blattbach River J1 increases its frequency because exfoliation joints occurred at this orientation (parallel to the valley axis). However, as in the case of J2, a second parallel set of fractures present evidences of tectonic origin (slickensides).

Set 3 (Table 2.10, Figure 2.9) dips towards the NE with steep angles (> 60 degrees). It has a similar frequency in the northern and southern domain (Fisher concentration about 4%). This set strikes perpendicular to the valley axis. It has been observed in both domains with more or less no variations in orientation.

Set 4 (Table 2.10, Figure 2.9) dips towards the NNE-SSW with steep to vertical angles (> 60 degrees), perpendicular to the valley axis. There is a slight variation in its strike between northern and southern domain (ca. 10 degrees). The frequency is higher in the northern domain (Fisher concentration about 4%) than in the southern domain (Fisher concentration about 2%).

2.5.2 DEM and GIS-based fracture investigations

In order to improve the spatial coverage of the locations sampled for fracture data, a DTM and GIS-based method was implemented. The small scale slope morphology in the Matter Valley is strongly controlled by the rock mass structure and rock walls follow discontinuity orientations (Figures 2.10 & 2.13). This fact along with the scarce or missing vegetation cover allows to indirectly extract discontinuity orientations from high resolution digital elevation models (HR-DEM).

Two HR-DEMs were available for this work, created by different methods. A 2.5 m model by digital photogrammetry techniques, created by the group of Photogrammetry and Remote Sensing ETH Zurich, from a set of 62 aerial photographs acquired in August 17th 2005 with orientation data from GPS measured control points, a derived point cloud of around 65 million points, and an accuracy of 0.5 to 1 m. The second model is a 2 m model derived from airborne-based LiDAR data created by SWISSTOPO available for areas up to 2000 m asl with a point spacing of less than 2 m and a vertical point accuracy better than 0.3 m.

Because of the way each DEM is created they present different characteristics. Kraus (2007) presents a brief summary of their characteristics. Photogrammetric models perform a geometrical reconstruction of an object in 3D from photographic images, where a photograph defines a bundle of rays or directions. A point on an object is reconstructed when the point is intersected from at least two directions. The directions or rays are generated by natural light and recorded by passive sensors (cameras). For LIDAR models 3D reconstruction is done by measuring objects (or point in objects) from a single location, collecting them as fields of directions and distances (polar coordinates plus azimuths). Position of the device at the moment of collection should be known (GPS/IMU information). Laser scanners are active sensors.

LIDAR based models present a higher accuracy for steep slopes because position is directly measured during data acquisition which brings real information for interpolation. However, accuracy of the model is strongly dependent on point density. For photogrammetry-based models to obtain the same accuracy, a substantial amount of processing is needed by manual control point addition/correction because the DEM construction is based on image matching and automatic object detection which generate an object-based point cloud. Usually just few points are placed automatically in steep slopes and they are often misplaced. Another significant advantage of using LIDAR models is that they obtain superior results in forested areas as they only need a single location measurement whereas the photogrammetry based models need to match a ground point in at least two images (forested areas are highly textured zones where changes in the position of the observer produce a strong change in the contrast of objects). Moreover, airborne based LIDAR models can remove forest expression from the models using only backscatter readings of last echoes which allows to build a real ground representation.

From field work it was observed that steep fracture sets often have a representation on the slope walls and that gentle dipping fracture sets represented on rock walls are usually covered by low vegetation (Fig. 2.10). Because of these two reasons, the airbone based LIDAR model was chosen due to its better accuracy on steep slopes and the possibility of having ground representation on forested areas. The influence of those factors in the area is described in a profile comparison of the area of Saenggini shown in Figure 2.11. For the upper part of the slope a difference in height in a relatively flat area is caused by the presence of vegetation (forest). In the photogrammetric model loss of features and flattening of walls are observed in the intermediate part of the slope where steeper walls are located. For the lower part of the slope, a difference in height is observed due to the presence of forest. Differences in height are in the order of 20 to 30 m.

To visualize the changes in slope orientation, a 3D color shaded relief map (Jaboyedoff, 2004) was derived from the LIDAR DEM using ArcGIS (Figure 2.12a). A series of built-in tools were used for its construction. A 3D color shaded relief map is a color-coded image based on HSV (Hue-Saturation-Value) color model showing changes in color according with the changes in slope orientation. In a HSV color model the color space is represented by a single cone (Figure 2.12b). Saturation is represented by the dip angle (slope). Hue corresponds to the dip direction angle (aspect). Value is assumed to be constant and equal to 90. Because ArcGIS can not build HSV images a transformation to RGB color model was carried out. Figure 2.12c shows a flowchart of the process. The RGB color model is represented by a Cartesian

coordinate system with each axis representing a primary color (red, green and blue). In order to get a better visualization of the changes, the color palette was inverted.

A careful selection of the DEM planes used for the fracture analysis was carried out taking in consideration that not all values in the 3D shaded relief image represent fracture orientations. Sampled areas were chosen trying to avoid the presence of artifacts. Presence of thick soil covers and overhanging blocks are the main source of errors. Thick soil covers are present in areas densely forested where last echoes LIDAR data recreate the ground topography but disguised rock exposure morphology (Figure 2.13a). Overhanging blocks hide rock walls to the sensor causing a deficient data collection and a wrong surface representation (Figure 2.13b). Selection of cells was done using 3D visualizations (an orthophoto mosaic created with aerial photographs acquired in 2005 was used as the top-most layer) and photographs of the slopes taken from different angles during the field data collection campaigns. Selected sampling areas (Figures 2.14) were digitized in ArcGIS. Values for dip and dip direction were individually extracted and exported in a matrix-shape ASCII format where cells outside of the selected areas where assigned a value of zero. The resulting files were converted to single column files in Microsoft Excel (as independent files for dip and dip direction) and exported to Rocscience DIPS to be plotted in stereonets (equal area, lower hemisphere). A total of more than 120'000 orientations were obtained. A source of bias was observed to result from the fact that steeply inclined surfaces are covered by a lower number of pixels than gentle inclined surfaces; a schematic representation is shown in Figure 2.15a. To correct the bias, areal correction was performed in a similar way as Terzaghi's correction.

Given a plane A, representing a surface with an area A equal to $l \times l$ (l is the pixel size) and inclination angle zero, a plane B with a similar area but an inclination angle equal to α, and a plane B' result of the projection of plane B on a flat surface (Figure 2.15b), we obtain:

$$B' = A \times \cos\alpha \tag{2}$$

Assuming A is equal to 1, then

$$W = \frac{1}{\cos\alpha} \tag{3}$$

Where W is the weight assigned to each orientation for correction, assuming that each orientation corresponds to a unit surface (pixel). Each orientation was repeated W number of times on the stereplots in order to correct the bias.

To investigate the detailed spatial variation of the fracture sets, the study area was divided in 10 sub-domains, each sub-domain corresponding to the area occupied by a single slope (Figure 2.1). Fisher distributions were used to observe clusters and group the data into sets. The new data collected helped to improve the spatial distribution of the information as it can be observed in Figure 2.14. A comparison between field data and the DEM derived data was carried out in order to validate the results.

2.5.3 Comparison between field and DEM-GIS-based fracture data

For comparison, field data was divided in the same 10 sub-domains as the DEM-GIS-based data and plotted in stereonets to cluster the data using Fisher distributions (Figures 2.16a & 2.16b). Measurements from each cluster were separated in their components (dip and dip direction) for further analysis. To assess the correspondence between data obtained from field work and DEMs, statistical analysis were performed. First, several distribution types for dip and dip direction, recommended in the literature, were compared and fitted to the field and DEM-based data. Second, distribution parameters for the previously chosen distribution were obtained for dip and dip direction of each set in every sub-domain for both field and DEM-based data. Finally, field data and DEM-based data were compared using statistical hypothesis testing (ANOVA index) in order to evaluate correspondence between the different sources.

2.5.3.1 Analysis of Orientation Distributions

Sixteen different types of distribution functions for dip and dip direction were analyzed in order to identify the best models for the orientation variations of the meso-scale discontinuity sets in the study area. For each sub-domain, fracture orientation data from DEM and field analysis were separated into the 4 inclined sets defined above using the code DIPS (Rocscience). The individual fracture orientations were then separated into their components (dip and dip direction) and evaluated using the program EasyFit, a standard application to fit probability distributions to sample data. The goodness of fit for distributions was evaluated using two different tests: Kolgomorov-Smirnov and Anderson-Darling. Kolmogorov-Smirnov (K-S) tests are used to decide if a sample comes from a population with a specific distribution. It is based on an empirical distribution function and calculates the largest vertical difference between the theoretical and the empirical cumulative distribution function. Anderson-Darling (A-D) tests are a modification of the K-S tests. This type of test gives more weight to the tails than K-S tests and does not depend on the specific distribution being tested. The fits of all sampled distributions were then ranked according to the K-S test and A-D test.

An example of the results for dip direction of J3 is shown in Table 2.7 and Figure 2.17 for the case of Walkerschmatt. This example is typical of the behavior presented for the other samples. Weibull, Normal and Gamma distributions are the distribution types that present the best results for both goodness of fit test K-S and A-D. The Uniform distribution scores well for K-S test but it has high P-values for A-D test because of the histogram following a Gaussian bell shape. Figure 2.18 shows a summary of the scores reached by the distributions for all samples extracted by DEM and field analysis. In total, 78 samples corresponding to ten sub-domains, 4 fracture sets per sub-domain, 2 samples each fracture set (DEM-based and field data samples), except for the case of Riedji where set 2 was not observed. The three best fit distribution types for all 78 samples where used to produce Figure 2.18. As mentioned before for K-S test, Weibull, Uniform, Normal and Gamma distributions are the ones that have the best fit representing 96% of the total. Weibull (2P and 3P) has a total of 41.5% of all highest scores, followed by Uniform (39.9%, continuous and discrete), Normal (14.1%) and Gamma (10.3%, 2P and 3P). Other distributions are not representative. For A-D tests Gamma distributions are the distribution that best fit the data with a

frequency of 37.5%, followed by Normal (25.2%), Weibull (22.2%) and Exponential (7.2%) being in total about 92% of the total.

Normal, Weibull and Gamma distributions are the best ranked for both tests. Normal distribution is consistently ranked in a high position while Weibull scores better for K-S test and Gamma does it for A-D test. Normal distribution is one of the three best fit distributions for 42.34% of the samples according to K-S test. This value rises to 75.68% for A-D test. Because of these results it was assumed for further analysis that samples follow normal distributions and subsequently their parameters were calculated for both field work and DEM based samples (Tables 2.8 to 11). It has to be mentioned that not all samples include all four reported fracture sets. Set 2 is persistently missed from the field work data samples in the sub-domains to the north of the Blattbach River but appears on the DEM based samples except for the case of Riedji. This fact can be related to the reduction in the frequency of fracture set 2 observed during field work recognition and to the small size of the samples collected during field work in the sub-domains to the north of the Blattbach River due to the difficult access to the area.

Distribution	Kolmogorov Smirnov		Anderson Darling
	Statistic	Rank	Statistic
Weibull (3P)	0.04777	1	1.984
Normal	0.05015	2	1.9497
Gamma (3P)	0.05486	3	1.8811
Uniform	0.05706	4	16.232
Weibull	0.06363	5	2.1767
D. Uniform	0.06699	6	341.54
Gamma	0.09404	7	3.9937
Neg. Binomial	0.12985	8	49.539
Exponential (2P)	0.23224	9	3.2611
Poisson	0.24074	10	795.62
Exponential	0.25063	11	3.5379
Geometric	0.26768	12	271.25
Logarithmic	0.49359	13	816.64
Binomial	No fit		
Hypergeometric	No fit		
Bernoulli	No fit (data max > 1)		

Table 2.7. Summary of statistics for several distribution types using dip direction set 3 sample acquired by DEM analysis for the area of Walkerschmatt.

2.5.3.2 Equivalence of field and DEM orientation distributions

To evaluate the equivalence between the fracture orientation data collected in the field with data extracted from DEM analysis a technique known as the "analysis of variance" (ANOVA) was used. This technique allows to study the homogeneity of a group of samples determining whether sample mean and

standard deviations can be considered as equal (null hypothesis) or not (alternate hypothesis) based on an analysis of the variance within and between samples. The variance is represented by:

$$SSTot = \sum_{i=1}^{N} (x_i - \bar{X})^2 \tag{4}$$

Sub-domain	Set 1		Set 2		Set 3		Set 4	
	Dip	Dip Direction	Dip	Dip Direction	Dip	Dip Direction	Dip	Dip Direction
Hohebalme	81.58	133.78	70.87	79.97	64.08	19.72	81.22	178.57
Guggini	81.25	123.17	71.38	75.82	76.11	24.58	80.10	179.02
Seemate	80.32	97.75	73.54	72.21	49.9	14.57	82.03	178.53
Saenggini	83.82	108.88	77.71	70.80	58.47	37.43	83.36	178.02
Walkerschmatt	76.67	116.20	74.37	77.82	65.71	24.85	81.97	192.29
Medji	73.52	11.16	65.09	72.40	75.89	47.43	75.58	165.58
Riedji	79.46	116.11	-	-	79.13	35.39	78.89	174.56
Saelli	68.62	117.54	75.54	72.21	68.13	25.88	78.67	171.91
Chalchofen	76.66	96.69	70.84	66.47	45.05	20.31	82.93	169.59
Sparru	63.80	126.23	58.63	68.77	62.29	25.95	78.11	170.99

Table 2.8. Mean values for orientation of meso-scale fracture samples extracted by DEM analysis.

Where SSTot corresponds to the sum of between samples squared deviations and within samples squared deviations for a set of k samples with:

Sample sizes $n_1, \ldots, n_k$

Sample means $\bar{x}_1, \ldots, \bar{x}_k$

Sample variances $s_1^2, \ldots, s_k^2$

Total count $N = \sum_{i=1}^{k} n_i$

Grand total observations $T = \sum_{i=1}^{k} n_i \bar{x}_i$

Grand mean of all observations $\bar{X} = \frac{T}{N}$

Alternatively, SSTot can be expressed as:

$$SSTot = \sum_{i=1}^{k} n_i(\bar{x}_i - \bar{X})^2 + \sum_{i=1}^{k}(n_i - 1)s_i^2 = BSS + ISS \quad (5)$$

Where BSS is the sum of between-sample squared deviations and ISS is the sum of within-sample squared deviations (Borradaile, 2003).

Sub-domain	Set 1		Set 2		Set 3		Set 4	
	Dip	Dip Direction	Dip	Dip Direction	Dip	Dip Direction	Dip	Dip Direction
Hohebalme	4.42	8.85	7.67	10.22	7.96	10.24	4.18	9.91
Guggini	5.56	10.99	6.88	7.39	5.31	5.97	5.55	8.76
Seemate	7.92	12.10	5.73	5.13	8.90	8.66	4.12	7.75
Saenggini	3.53	11.65	3.08	4.10	12.40	13.80	3.48	5.88
Walkerschmatt	5.96	10.85	6.58	7.98	6.90	11.17	5.88	9.80
Medji	6.79	11.28	5.14	6.72	5.94	7.75	6.91	7.80
Riedji	3.43	12.97	-	-	4.13	6.81	6.40	10.18
Saelli	7.55	10.01	5.73	5.13	6.76	9.76	5.98	10.06
Chalchofen	4.67	7.38	6.04	6.77	6.90	9.77	4.46	8.21
Sparru	7.07	12.31	6.36	8.06	7.40	10.80	5.77	5.98

Table 2.9. Standard deviation values for orientation of meso-scale fracture samples extracted by DEM analysis.

The ANOVA test was carried out for each pair of samples for all fracture sets in all sub-domains (k value of 2 for two samples for every population). The null hypothesis is set as if samples come from a population with the same mean (Ho: $\bar{x}_1 = \bar{x}_2$). The alternative hypothesis is that their means differ from each other (Ha: $\bar{x}_1 \neq \bar{x}_2$). The test for this case is a ratio between the variances between-samples and within-sample with degrees of freedom V1=1 and V2 = N-2. The F-distribution for this case is:

$$F = \frac{\frac{BSS}{ISS}}{N-2} \quad (6)$$

F-distribution values were calculated for all cases where data from both sources were available (Table 2.12) and compared with the critical value of 3.84 for a confidence level (α) of 0.05 (Borradaile, 2003). 3.84 corresponds to the critical value assigned to samples with V2>120. F-distribution values vary between 0.0006 and 5.62. Only in one case Ho is not accomplished (Saenggini dip direction set 4, F-distribution value of 5.62), i.e. only at for set 4 at Saenggini the orientation distributions derived in the field and from DEM analysis differ significantly.

Sub-domain	Set J1		Set J2		Set J3		Set J4	
	Dip	Dip Direction	Dip	Dip Direction	Dip	Dip Direction	Dip	Dip Direction
Hohebalme (S)	80.25	126.65	69.64	77.52	67.78	22.56	82.00	161.63
Guggini	75.38	125.08	69.41	71.73	-	-	82.17	174.50
Seemate	79.67	120.89	65.50	66.22	76.64	17.57	80.6	169.2
Saenggini	81.79	120.57	74.37	77.82	66.70	31.84	80.0	215.0
Walkerschmatt	80.55	102.13	70.125	69.94	68.59	32.94	83.29	195.71
Medji	80.92	100.4	68.82	68.72	72.22	33.04	81.4	197.0
Riedji	70.09	106.91	-	-	73.75	36.75	78.25	181.75
Saelli	55.5	118.56	-	-	66.71	29.0	77.2	172.87
Chalchofen	-	-	-	-	-	-	-	-
Sparru (N)	63.0	119.88	64.29	82.57	54.4	10.8	81.8	181.0

Table 2.10. Mean values for orientations of meso-scale fractureses collected during field work (Subdomains are listed from South to North).

Sub-domain	Set 1		Set 2		Set 3		Set 4	
	Dip	Dip Direction	Dip	Dip Direction	Dip	Dip Direction	Dip	Dip Direction
Hohebalme	6.65	4.11	5.06	5.66	10.28	6.52	6.30	5.53
Guggini	4.43	8.46	6.71	6.26	-	-	6.97	73.88
Seemate	6.71	6.68	5.84	9.41	7.25	6.69	5.13	5.63
Saenggini	5.04	6.42	6.58	7.38	8.44	8.54	3.30	10.34
Walkerschmatt	6.06	6.14	3.53	8.11	6.11	9.24	3.50	4.64
Medji	6.09	6.16	6.58	5.86	6.19	8.01	5.32	4.64
Riedji	6.63	15.66	-	-	6.85	7.89	8.26	8.46
Saelli	7.32	12.41	-	-	5.77	9.42	8.56	45.50
Chalchofen	-	-	-	-	-	-	-	-
Sparru	5.53	8.08	4.53	8.86	5.68	6.14	7.05	5.66

Table 2.11. Standard deviation values for orientation of meso-scale fracture samples collected during field work.

Set 1 (J1) dips with values ranging from 63 to 81. A clear decrease in the steepness is observed from S to N. A sharp change is observed at the Blattbach River where dip angle decreases 7 degrees. Set 1 dips towards the SE to the S of the study area and rotates counterclockwise, dipping to the E in the Saenggini sub-domain. From Saenggini to the N, dip direction is about 115° until the study area limits. At Sparru, dip direction rotates towards the SE, getting a similar orientation as in the southern part of the area.

Set 1 (J1) dips with values ranging from 63 to 81. A clear decrease in the steepness is observed from S to N. A sharp change is observed at the Blattbach River where dip angle decreases 7 degrees. Set 1 dips towards the SE to the S of the study area and rotates counterclockwise, dipping to the E in the Saenggini sub-domain. From Saenggini to the N, dip direction is about 115° until the study area limits. At Sparru, dip direction rotates towards the SE, getting a similar orientation as in the southern part of the area.

Set 2 (J2) dips with angles between 58 and 71 degrees. There is no well defined trend for the whole area. The lower dip angle values are found to the N of the Blattbach River in Medji and Sparru sub-domains. This fracture set dips toward the NNE for the whole area. A small counterclockwise rotation is observable from S to N in the study area. A peak in the dip direction angle value is found at Walkerschmatt, right after the Blattbach River.

Set 3 (J3) dips consistently to the NNE-E with moderate to steep angles. There is not a transitional change in the orientation into the study area. However, there are strong variations from one sub-domain to the other. Steeper dip angles are found in the central part of the study area (between Saenggini and Riedji).

Sub-domain	Set 1		Set 2		Set 3		Set 4	
	Dip	Dip Direction	Dip	Dip Direction	Dip	Dip Direction	Dip	Dip Direction
Hohebalme	0.018	0.033	0.01	0.013	0.02	0.006	0.02	0.24
Guggini	0.47	0.003	0.04	0.12	-	-	0.02	0.0006
Seemate	0.001	0.23	1.05	0.78	1.57	0.02	0.03	0.12
Saenggini	0.36	0.10	1.97	3.46	0.13	0.04	0.38	5.62
Walkerschmatt	0.45	0.54	0.15	0.30	0.12	0.14	0.01	0.009
Medji	0.63	0.18	0.20	0.07	0.24	1.25	0.07	1.33
Riedji	3.55	0.02	-	-	0.38	0.003	0.001	0.02
Saelli	0.84	0.001	-	-	0.007	0.007	0.02	0.0001
Chalchofen	-	-	-	-	-	-	-	-
Sparru	0.002	0.014	0.14	0.31	0.10	0.08	0.12	0.77

Table 2.12. F-distribution values calculated using the ANOVA technique for the meso-scale fracture sets.

Set 4 (J4) dips steeply to the S having a small clockwise rotation from S to N of the study area (seven degrees). The highest variation on dip direction is observed at the Walkerschmatt sub-domain with a

difference of about 15 degrees respect to the main trend. Dip angle values remain similar for the whole study area.

Sub-domain	Set 1		Set 2		Set 3		Set 4	
	Dip	Dip Direction	Dip	Dip Direction	Dip	Dip Direction	Dip	Dip Direction
Hohebalme	81.58	133.77	70.85	79.95	64.14	19.76	81.22	178.49
Guggini	81.21	123.19	71.35	75.75	76.11	24.58	80.12	178.99
Seemate	80.32	97.81	73.39	72.10	50.60	14.65	82.02	178.50
Saenggini	83.81	108.91	77.60	71.038	58.53	37.39	83.35	178.12
Walkerschmatt	76.73	116.00	74.28	77.63	65.76	24.98	81.98	192.30
Medji	73.66	110.95	65.20	72.29	75.72	46.76	75.62	165.78
Riedji	79.40	116.06	-	-	79.08	35.40	78.89	174.58
Saelli	67.66	117.61	75.54	72.21	68.11	25.91	78.63	171.94
Chalchofen	76.66	96.69	70.84	66.47	45.05	20.31	82.93	169.59
Sparru	63.79	126.15	58.69	68.92	62.23	25.81	78.20	171.24

Table 2.13. Summary of mean values for meso-scale fracture set orientations. Black figures correspond to grand mean values and blue figures to only DEM based values.

2.6 Large Scale Fractures (Faults)

2.6.1 Field Investigations

Four main sets of large scale fractures were found and described during field recognition. For this work 81 orientations of discontinuities collected by Zuger (2007) have been included for the stereoscopic analysis. 145 additional large scale fractures were identified and described during field recognition for the present work. A stereoplot showing fracture orientations is shown in Figure 2.19. The sets present some similarities to descriptions found in the local literature (Section 4). The sets comprise fractures characterized as faults, fracture zones and brittle-ductile shear zones. Descriptions follow the nomenclature presented by Willenberg et al. (2008). A fault is characterized as a structure with a significant differential displacement. Fracture zones are described as wide areas with intense brittle fracturing but minor differential displacement. Ductile shear zones correspond to densely foliated and fine-grained schists and gneisses (mainly phyllonites and mylonites). Ductile shear zones in the study area often have undergone subsequent brittle deformation and are called brittle-ductile shear zones.

Set 1 (F1; 220/13) corresponds to large scale fractures parallel to foliation (Figure 2.19). This set presents a high level of spatial scattering gradually varying its orientation from S to N. F1 has been described briefly

in chapter 4. Set 2 (F2; 010/46) is mainly composed by faults and fracture zones. A specimen of this set has been identified by Sartori et al. (2003) to be the basal plane for the failure of April 1991 at Randa. F2 faults can have traces of several hundred of meters with thick clay gouges and cataclasites (Figure 2.20). Set 3 (F3; 077/68) correspond to faults with slickensides and chlorite infillings that on field have been found to have traces between 5 to 100 m. This set corresponds to set F30 from Gischig et al. (submitted), one of the fractures from this set works as the lateral release plane of the current instability at Randa. Willenberg et al. (2008) argue that fractures of this set can be clearly observed on aerial images with traces that can reach 100m. Most of the larger structures are fracture zones i.e. areas with a high frequency of fractures. This set is parallel to the meso-scale fracture set J2 presented above for the southern part of the study area. Towards the N, fracture zones with this orientation are less frequent. However, some fracture zones are still observed in the northern region of the area but with a slightly different orientation, following set J1. Persistence and frequency of this set increase towards the N. Set 4 (F4) are steep faults with fine grained gouge infillings (clay) in the paragneiss, and fracture zones following discontinuities of meso-scale set J4 in the orthogneiss. Discontinuities from this set can have lengths in the order of tens to hundreds of meters. Figure 2.21 shows examples of all four sets for the area.

2.6.2 DEM-based extraction of large scale lineaments

Approximately 650 lineaments that were assumed to correspond to large fractures were identified and mapped during field work from the other side of the valley and digitized in ArcGIS as polylines (Figure 2.21). Other lineaments were added based on interpretation of digital aerial photographs taken in 2005. Lineament traces were modified in order to fit to morphological features observed on the 3D shaded relief map. Lineaments that did not have a morphological expression in the DEM were discarded. All lineaments shorter than 100 m were discarded assuming that they do not correspond to what was defined as large scale discontinuity in the present work. A total of 350 lineaments were kept for further analysis. 3D coordinates for the vertices of the lineaments (x,y,z coordinates) were calculated based on the high resolution digital elevation models described previously and processed with a script written in Matlab to calculate the best fit plane for each lineament by multiple regression using least squares methods. The code calculates the direction cosines for the normal vector to the best fit plane based on at least 3 vertices. Using the direction cosines as input coordinates, dip and dip direction for each lineament were calculated by vector geometry.

The results show a small clockwise rotation of the F2 fracture set (Figure 2.22) and a reduction of the dip angles of the steep sets (F3 and F4) with respect to the field data. Rotation varies between 5° and 15°. Reduction in the dip angle is about 10° for the case of set F3. Only few planes from Set F1 are observable in the DEM. This can be explained by the fact that they usually do not have a morphological expression (planes dip into the slope). There is significantly higher scattering than in the field derived orientation data. This has already been previously reported by other authors (e.g.: Lato et al., 2009, Sturzenegger & Stead, 2009) and related to the waviness of the fault plane and to the position of the fracture traces with respect to the position of the laser scanner during acquisition. Fracture sets parallel to the line of sight of

the device present higher errors in their orientation values. Length of the lineaments plays a role in the quality of the orientation results too. In spite of all these sources of errors, the three inclined large scale fracture sets could be clearly recognized and clustered (Figure 2.22). Similar to what has been observed with the meso-scale fracture sets (Chapter 5), there is a difference between the geometrical characteristics of large scale fracture sets between the northern and southern areas (Figures 2.23a and 2.23b). A clear limit again is the Blattbach River. DEM-derived large scale fractures to the South of the Blattbach River present a spatial distribution comparable to what has been observed during field work. The four main sets can be clearly differentiated. To the North, differences between sets are less obvious. Lineaments representing structures parallel to foliation were not found. Besides the clusters related with the large scale discontinuity sets, there is a concentration of values similar in orientation to the meso-scale fracture set J1 in the northern region. This could be explained by the increasing persistence of J1 fractures to the N of the Blattbach River, leading to trace lengths bigger than hundred meters, which is the cut-off for large scale lineaments in this work. As it can be observed on Figures 2.23a and 2.23b, current morphology of the slopes has a strong structural control. To the area to the N of the Blattbach River large scale structures have a strong influence in the morphological configuration.

2.7 Discussion

2.7.1 Methodology

The study area of this project shows a very rugged and steep topography which makes field investigations of fracture pattern a time-consuming and risky endeavor. For such areas new applications of GIS-based techniques are presented here. These techniques benefit of the recent development of new methodologies for DEM generation via new remote sensing devices (e.g. airborne-based LIDAR) and improvements on more traditional techniques (e.g. digital aerial photogrammetry) which allows the generation of more accurate and detailed DEMs (increase on position and resolution). For the application of the techniques presented here, high resolution DEMs and optical images are needed in order to obtain reliable results. This is more evident for the characterization of meso-scale fractures. In areas with high relief such as the Matter Valley, steep slopes are still affected by artifacts e.g. exaggeration on rockwall dip angle caused by overhanging blocks. A manual selection of sample sites is required. It has been done for the present work through field recognition and analysis of optical images (photographs). Comparison between field values and DEM extracted values show high level of correspondence. Results obtained by the application of ANOVA gives a good correlation.

2.7.2 Discontinuity Inventory

Discontinuities are the most important factor for the development of instabilities in hard rocks, especially for the study area in the western flank of the Matter Valley. Both, meso-scale and large scale discontinuities have controlled former past events like the ones occurred at Randa and Medji.

In the study area foliation is generally expressed as schistosity. Schistosity dips into the slope with a clear variation on its values. Schistosity varies along height and on a planimetric perspective (from S to N). In the southern half of the area, the spatial variation on its orientation exists from S to N and from bottom to top of the slopes. Close to the valley bottom, foliation dips persistently to the S with angles varying between 190° and 210°. It transitionally rotates clockwise dipping to the SW at the top end of the slopes. The maximum rotation is reached to the southern limit for the Randa (Grossgufer) and Hohebalme slopes. The other slopes to the S (Guggini, Seemate and Saenggini), follow a similar trend but with a slighter rotation. Dip angle values are higher to the bottom of the slopes and smoothly change upwards. Smaller values of dip are found on Randa, Hohebalme and Guggini. For the other two slopes in the S, the trend in the spatial distribution of the dip angles is similar.

A clear change in the behavior of the foliation is observed at the Blattbach River. To the N of the Blattbach River, there is no clear difference in orientations between bottom and top of the slopes. Medji can be considered as a clear bending point in the values of dip direction of foliation. As in the southern half of the area, to the S of Medji mean dip direction is towards the SW while to the N of Medji, foliation dips recurrently to the W-NNW. At the limit of the area (Sparru), a perceptible difference between bottom and top of the slope is observed. Bottom of the slope dips to the W, while to the top dips to the NW. Dip angle values have a clear change at the area of Medji. To the S (Walkerschmatt), foliation dips gently with angles between 12° to 20° whereas to the N, dip angle raises up to more than 35 degrees to the NW of the area.

For this work, non-penetrative discontinuities parallel to the foliation in the area have been divided in two classes. A meso-scale fracture set that has been observed as well by other authors (Wagner 1991; Willenberg, 2004) and a large scale set composed by ductile shear zones reactivated by brittle processes. The spatial distribution of these two sets cannot be clearly defined. They are present along the whole area, but spacing, persistence and other characteristics greatly vary along the area.

The other non-penetrative discontinuities were classified according to their persistence in meso and large scale discontinuities. They are basically brittle discontinuities that can be differentiated as joints, faults, shear zones and fracture zones. For the area joints are mainly meso-scale fractures; faults and fracture zones are large scale fractures. However, towards the N, especially after the Blattbach River, some joints can have persistence values up to hundred meters which should be classified as large scale fractures. However, for the present analysis fracture sets that were identified as meso-scale fractures in the southern part of the area were not later reclassified as large scale fractures in order to keep the coherence in the classification. In the case of fault and fracture sets, some faults and fracture zones can have persistence values of only few tens of meters, but they are simple specimens distributed along the whole study area and do not represent persistent changes in the characteristics of the fracture sets.

Four main meso-scale fracture sets have been found in the area, which have been described in detail above. They present clear spatial patterns and are persistent along the whole area. Spatial variation in their orientation values does not to follow a regular pattern. Some of the fracture sets present a slight clockwise rotation towards the N, but for some others a clear variation cannot be observed and it can even be considered random. This fact can be explained as a result of the high heterogeneity that fractures in general possess (Tran, 2007) and by the intrinsic errors and biases that databases in general have.

However, a clear change in the relationships between sets can be observed at the Blattbach River. Frequency of fracture set drastically changes, especially for sets J1 and J2. To the South, J2 is the most frequent set found in all datasets (spot and lineal mapping and DEM-based extraction data). To the N, contrarily, J1 becomes the most frequent set. As mentioned above, this change can have a connection with the rotation of the valley axis after the Blattbach River, which causes the migration of the exfoliation joints parallel to the valley axis from set J2 to set J1.

A variation in the number and distribution of fractures not related with the main sets is observed for the area. To the S, in the sub-domains Randa, Hohebalme and Guggini a higher number of clusters exist and they are clearly observed within the field data and are slightly perceptible on the DEM-based data. That situation is due to the geometrical disposition of those fractures sets respect to the slope. Most of the above mentioned fracture sets are dipping into the slope and do not have a morphological expression on the current topography, in a similar manner to the conditions mentioned for the fractures parallel to the foliation. Therefore, they cannot be observed on the 3D shaded relief map and have a small representation in the DEM-based datasets. Other authors have reported up to 10 meso-scale fracture sets for those areas (Wagner, 1991; Willenberg, 2004). The increase in the complexity of the structural pattern for this part of the area can be related to two main factors: A first factor is the change on the lithological conditions respect to the rest of the area. At the area of the current instability on Randa (Grossgufer), the presence of ortho- and para-gneisses has been reported by several authors (Bearth, 1964; Wagner, 1991; Sartori et al., 2003; Willenberg, 2004). Whereas northwards, the area comprises mainly orthogneisses (the Randa Augengneiss). Paragneisses present a more irregular fracture network (Gischig et al., submitted).

The proximity to the confluence of the valley formed by the Bisgletscher glacier with the Matter Valley is considered a second factor of importance. Glaciations increase the load that rock slopes undergo causing gradual rock mass dilation (stress release), which causes, among other effects, propagation of the internal joint network (Ballantyne, 2007). A last factor only affecting the area of the current instability at Randa is the generation of secondary fractures product of intact rock bridges breakage caused by the strong deformation that the slope undergoes. Towards the northern limit of the study area, at Sparru, there is again a change on the lithology with sequences of mica-schists and quarzites to the bottom of the slope overlaid by ortho-gneisses in the middle part of the slope and para-gneisses to the top (above 2300 m asl). This lithological variation causes a more complex fracture network in a similar way that what have been mentioned for the area of Randa, Hohebalme and Guggini.

Three main large scale fracture sets have been found in the area (besides an additional set, F1, parallel to foliation, mentioned before). F2 is composed basically by faults with gouge. F3 fractures are mainly fracture zones and it is similar in orientation to meso-scale fracture set J2. Faults and fracture zones are part of fracture set F4. Plane extraction from lineaments mapped during field work, image interpretation and DEM analysis show a similar trend. There is clear limit on the spatial disposition of the fracture sets at the Blattbach River. Large scale structures strongly control the current morphology to the North.

2.7.3 Implications for slope stability

An approach to slope stability for the area was carried out by a classification of the relationship between orientation of foliation and slope geometry. A classification proposed by Meentemeyer (2000) was used, which defines seven different classes. Cataclinal slopes have a higher probability of failure than the others classes (Cruden, 2003), being overdip slopes the sub-class with the highest probability of planar failure along the fractures parallel to foliation. Overdip slopes for the area, are mostly the south-faced slopes found to the S of Medji. According with Cruden (2003) toppling can as well be possible if further conditions are present (a second set of fractures dipping into the slope perpendicular to foliation).

Spatial variations of fracture characteristics as well as morphology of slopes have a strong influence on the stability. A higher level of activity is observed to the N of the Blattbach River, being morphologically expressed by a higher volume of debris deposits to the base of the slopes (Figures 2.23a and 2.23b). This limit coincides with the change of meso and large scale fracture characteristics. The analysis of the rock slope stability is presented in a companion paper.

2.8 Summary

A detail structural characterization for the western flank of the Matter Valley has been carried out for the present work. It has been focused in two of the main characteristics that fractures possess: orientation and length. Discontinuities have being divided on penetrative and non-penetrative. Penetrative discontinuities are represented by foliation in the area. Non-penetrative discontinuities comprise joints, faults, shear zones and fracture zones. Non-penetrative discontinuities have been sub-divided on meso and large scale discontinuities based on their length. Spatial variation on their orientation has been observed through a detailed analysis of data. GIS systems have been used to extract information from remote sensing imagery interpretation and DEM analysis. Reliability of these data has been tested by comparison with the field data using classic statistics, giving an acceptable matching.

Penetrative discontinuities have a uniform variation from S to N and from bottom to top of the slopes. Foliation has been divided in five domains based on its variation on orientation. Two sets of non-penetrative discontinuities are associated to foliation and present the same trend as foliation on their orientation. The rest of non-penetrative discontinuities present differences in their pattern between the northern and the southern parts of the area. Four main sets of meso-scale fractures and three sets of large scale fractures (additional to the sets parallel to foliation) have been found and described. A limit between southern and northern domains is located at the Blattbach River. The variation on the fracture set pattern seems to be partially linked to the rotation of the valley axis (15°, clockwise) what causes that exfoliation joints rotates in a similar manner. Variation in other fracture characteristics and other fracture sets may be related with regional tectonics. Local variations in the fracture pattern are linked with lithological changes.

Changes in the fracture network configuration have a relation with slope stability. To the N of the Blattbach River, slopes have a higher level of rock fall activity than to the S due to the structural predisposition.

2.9 References

Agliardi, F., Crosta, G., and Zanchib, A., 2001, Structural constraints on deep-seated slope deformation kinematics: Engineering Geology, v. 59, p. 83-102.

Augustinus, P.C., 1992, The influence of rock mass strength on glacial valley cross-section morphometry: a case study from the Southern Alps, New Zealand: EARTH SURFACE PROCESSES AND LANDFORMS, v. 17, p. 12.

Ballantyne, C.K., 2002, Paraglacial geomorphology: Quaternary Science Reviews, v. 21, p. 1935-2017.

Ballantyne, C.K ., 2007, Paraglacial Geomorphology, Periglacial Landforms, p. 2170-2182.

Borradaile, G., 2003, Statistics of earth science data: Berlin, Springer-Verlag, 351 p.

Brady, B.H.G., and Brown, E.T., 2004, Rock mechanics for underground mining: London, Kluwer Academic Publishers, 626 p.

Brideau, M.-A., Stead, D., and Couture, R., 2006, Structural and engineering geology of the East Gate Landslide, Purcell Mountains, British Columbia, Canada: Engineering Geology, v. 84, p. 24.

Brideau, M.-A., Yan, M., and Stead, D., 2009, The role of tectonic damage and brittle rock fracture in the development of large rock slope failures: Geomorphology, v. 103, p. 20.

Bussy, F., Sartori, M., and Thélin, P., 1996, U-Pb zircon dating in the middle Penninic basement of theWestern Alps (Valais, Switzerland): Schweizerische Mineralogische und Petrographische Mitteilugen, v. 76, p. 4.

Cruden, D.M., 1989, Limits to common toppling: Can. Geotech. J., v. 26, p. 6.

Cruden, D.M., 2003, The shapes of cold, high mountains in sedimentary rocks: Geomorphology, v. 55, p. 13.

Eberhardt, E., Stead, D., Coggan, and S., J., 2004, Numerical analysis of initiation and progressive failure in natural rock slopes - the 1991 randa rockslide: International Journal of rock Mechanics and Mining Sciences v. 41, p. 20.

Escher, A., 1998, Structure de la nappe du Grand Saint-Bernard entre le val de Bagnes et les Mischabel: Rapp. géol. Serv. hydrol. géol natl, v. 7.

Feng, Q., Sjögren, P., Stephansson, O., Jing, L., 2001, Measuring fracture orientation at exposed rock faces using a non-reflector total station: Engineering Geology, v. 59, p. 133-146.

Genier, Florian, Epard, Jean-Luc, Bussy, Francois, Magna, and Tomas, 2008, Lithostratigraphy and U-Pb zircon dating in the overturned limb of the Siviez-Mischabel nappe: a new key for Middle Penninic nape geometry: Swiss Journal of Geosciences, v. 101, p. 22.

Girod, F., 1999, Alterátion Météorique de roche granitique en milieu alpin: le cas de l'orthogneiss associé à l'éboulement de Randa (Mattertal, Valais, Suisse): Lausanne, Université de Lausanne.

Gischig, V., Loew, S, A., K., R., M.J., Raetzo, Hugo, and F., L., 2009, Identification of active release planes using ground-based differential INSAR at the Randa rock slope instability, Switzerland: Natural Hazards and Earth System Sciences, v. 9, p. 12.

Gischig, V., Ammann, F., Moore, J. R., Loew, S., Eisenbeiss, H., Stempfhuber, W., Submitted, Composite rock slope kinematics at the current Randa instability, switzerland, based on remote sensing and numerical modeling: Engineering Geology.

Jaboyedoff, M., Couture, R., 2003, Report on the project COLTOP3D for March 2003: stay of Michel Jaboyedoff at GSC-Ottawa. Quanterra administrative document – Activity report – RA01.

Jaboyedoff, M., Baillifard, F., Couture, R., Locat, J., and Locat, P., 2004, New insight of geomorphology and landslide prone area detection using digital elevation model(s), in Lacerda, Ehrlich, Fontoura, and Sayão, eds., Landslides: Evaluation and Stabilization: London, Taylor & Francis Group, p. 6.

Joerg, and Tobias, 2008, Versagensmechanismus und Disposition des Medji Felssturz (Mattertal, Wallis): Zurich, ETH Zurich.

Kelly, M.A., Buoncristiani, J.F., and Schlüchter, C., 2004, A reconstruction of the last glacial maximum (LGM) ice-surface geometry in the western Swiss Alps and contigous Alpine regions in Italy and France: Ecoglae geol. Helv., v. 97.

Ladner, F., Rovina, H., Pointner, E., Dräyer, B., and Sambeth, U., 2004, Ein angekündigter Felssturz. Geologische Überwachung und Instrumentierung des Felssturzes «Medji» bei St. Niklaus (Wallis), tec21, Volume 27-28, p. 10-14.

Lato, M., Diederichs, S., M., Hutchinson, J., D., Harrap, and R., 2009, Optimization of LiDAR scanning and processing for automated structural evaluation of discontinuities in rock masses: International Journal of Rock Mechanics & Mining Sciences, v. 46, p. 6.

Loew, S., Willenberg, H., Spillmann, T., Heincke, B., Maurer, H.R., Eberhardt, E., and Evans, K., 2007, Structure And Kinematics Of A Large Complex Rockslide As Determined From Integrated Geological And Geophysical Investigations (Randa, Switzerland), 1st North American Landslide Conference Vail: AEG Special Publication 23.

Markley, M.J., Teyssier, C., and Caby, R., 1999, Re-examining Argand's view of the Siviez-Mischabel nappe: Journal of Structural Geology, v. 21, p. 6.

Markley, M.J., Teyssier, C., Cosca, M.A., Caby, R., Hunziker, J.C., and Sartori, M., 1998, Alpine deformation and $^{40}Ar/^{39}Ar$ geochronology of synkinematic white micas in the Siviez-Mischabel Nappe, western Penninic Alps, Switzerland: Tectonics, v. 17, p. 18.

Mazzoccola, F., D., Hudson, and A., J., 1996, A comprehensive method of rock mass characterization for indicating natural slope instability: Quarterly Journal of Engineering Geology and Hydrogeology, v. 29, p. 21.

Meentemeyer, R.K., and Moody, A., 2000, Automated mapping of conformity between topographic and geological surfaces: Computers & Geosciences, v. 26, p. 15.

Milnes, A.G., Hudson, J., Wikström, L., and Aaltonen, I., 2006, Foliation: Geological Background, Rock Mechanics Significance, and Preliminary Investigations at Olkiluoto: OLKILUOTO, FINLAND.

Palmström, A., and Singh, R., 2001, The deformation modulus of rock masses - comparisons between in situ tests and indirect estimates: Tunnelling and Underground Space Technology, v. 16, p. 17.

Powell, J.W., 1875, Exploration of the Colorado river of the West and its tributaries, explored in 1869-72: Washington, DC, Government Printing Office.

Priest, S. D., 1993, Discontinuity analysis for rock engineering: London, Chapman & Hall, 473 p.

Roullier, J.D., Jaboyedoff, M., Marro, C., Philipposian, F., and Mamin, M., 1998, Pentes instables dans le Pennique valaisan. MATTEROCK: une méthodologie d'auscultation des falises et de détection des éboulements majeurs potentiels: Zurich, Hochschulverlag AG, 239 p.

Sander, B., 1970, An introduction to the Study of the fabric of the Geological Bodies: Oxford, Oxford University Press.

Sartori, M., Gouffon, Yves, Marthaler, and Michel, 2006, Harmonisation et définition des unités lithostratigraphiques briançonnaises dans les nappes penniques du Valais: Ecoglae geol. Helv., v. 99, p. 46.

Sartori, M., Baillifard, F., Jaboyedoff, M., and Rouiller, J.D., 2003, Kinematics of the 1991 Randa rockslides (Valais, Switzerland): Natural Hazards and Earth System Sciences, v. 3.

Schindler, C., Cuénod, Y., Eisenlohr, T., and Joris, C.L., 1993, Die Ereignisse vom 18. April und 9. Mai 1991 bei Randa (VS) - ein atypischer Bergturz in Raten: Ecoglae geol. Helv., v. 86, p. 23.

Schindler, C., and Eisenlohr, T., 1992, Bergsturz Grossgufer bei Randa: Geologisch-geotechnische Expertise: Zurich, p. 83.

Segalini, A., and Giani, G.P., 2004, Numerical Model for the Analysis of the evolution mechanisms of the Grossgufer rock slide: Rock Mechanics and Rock Engineering, v. 37, p. 18.

Sturzenegger, M., and Stead, D., 2009, Close-range terrestrial digital photogrammetry and terrestrial laser scanning for discontinuity characterization on rock cuts: Engineering Geology, v. 106, p. 20.

Thélin, and Ph., 1987, Nature originelle des gneiss oeillés de Randa (Nappe de Siviez-Mischabel, Valais): Lausanne, 75 p.

Tran, N.H., 2007, Fracture orientation characterization: minimizing statistical modelling errors: Computational statistics & data analysis, v. 51, p. 10.

Turner, F.J., and Weiss, L.E., 1963, Structural analysis of metamorphic tectonites: New York, McGraw-Hill.

Webster, R., and Oliver, M.A., 1989, Optimal interpolation and isarithmic mapping of soil properties. VI. Disjunctive kriging and mapping the conditional probability: Journal of Soil Science, v. 40, p. 16.

Willenberg, and H., 2004, Geologic and kinematic model of a complex landslide in crystalline rock (Randa, Switzerland) [PhD. Thesis thesis]: Zurich, Swiss Federal Institute of Technology.

Willenberg, H., Loew, Simon, Eberhardt, E., Evans, F., K., Spillmann, Thomas, Heincke, B., Maurer, R., H., Green, and G., A., 2008, Internal structure and deformation of an unstable crystalline rock mass above Randa (Switzerland): Part I - Internal structure from integrated geological and geophysical investigations: Engineering Geology, v. 101, p. 14.

Winistorfer, J., 1977, Paléogéographie des stades glaciaires des vallées de la rive gauche du Rhone entre Viège et Aproz(VS): Sion, Université de Lausanne.

Yates, S.R., Warrick, A.W., and Myers, D.E., 1986, Disjunctive kriging 1. Overview of estimation and conditional probability: Water Resources Research, v. 22, p. 7.

Zangerl, C., Löw, S., and Eberhardt, E., 2006, Structure, geometry and formation of brittle discontinuities in anisotropic crystalline rocks of the Central Gotthard Massif, Switzerland: Ecoglae geol. Helv., v. 99, p. 20.

Zueger, D., 2007, Stabilitätsuntersuchungen der westlichen Talseite des Mattertals zwischen Randa und Mattsand und Vergleiche mit den Ereignissen von 1991 und der heutigen Instabilität in Randa (Schweiz): Zurich, ETH Zurich.

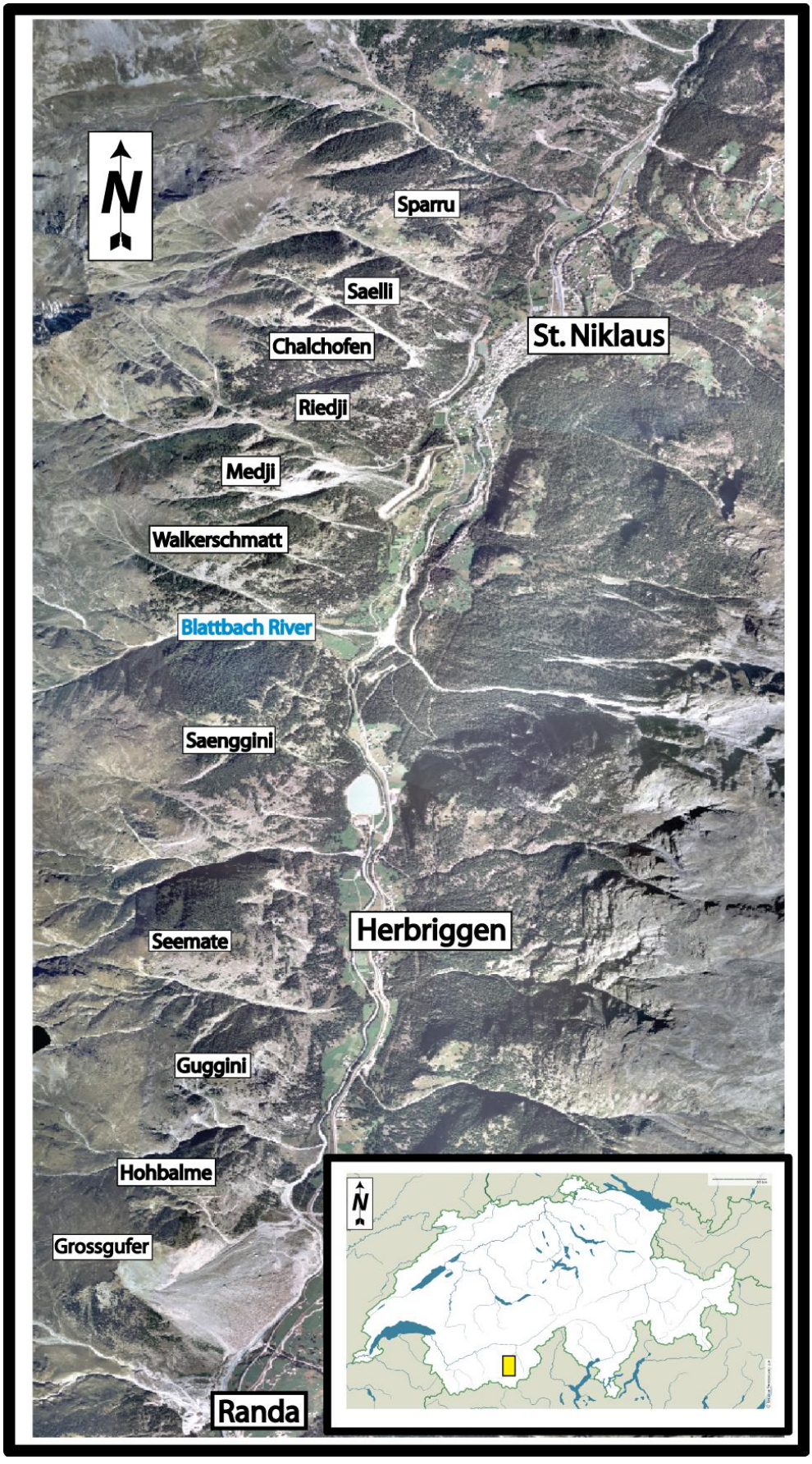

Figure 2.1. Situation Map of the study area.

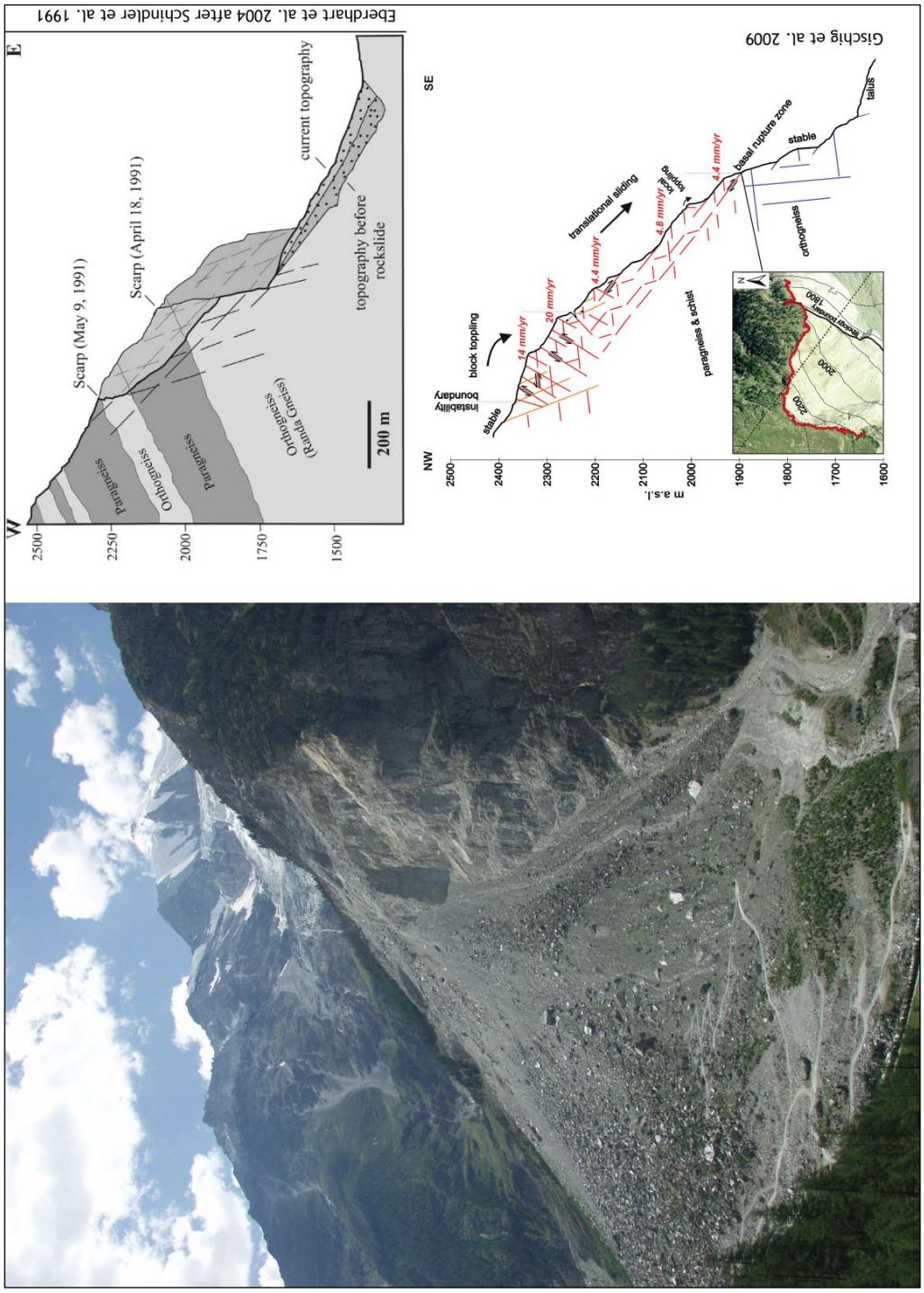

Figure 2.2. Randa rockslides. a) Photograph of 1991 failure surface and deposits, current situation. b) Schematic representation of the situation before 1991 and the geometric disposition of the two failed masses of April and May 1991 (from Eberdhardt et al., 2004). c) Cross section through the current unstable mass in the northern part of the 1991 scarp (from Gischig et al., 2009)

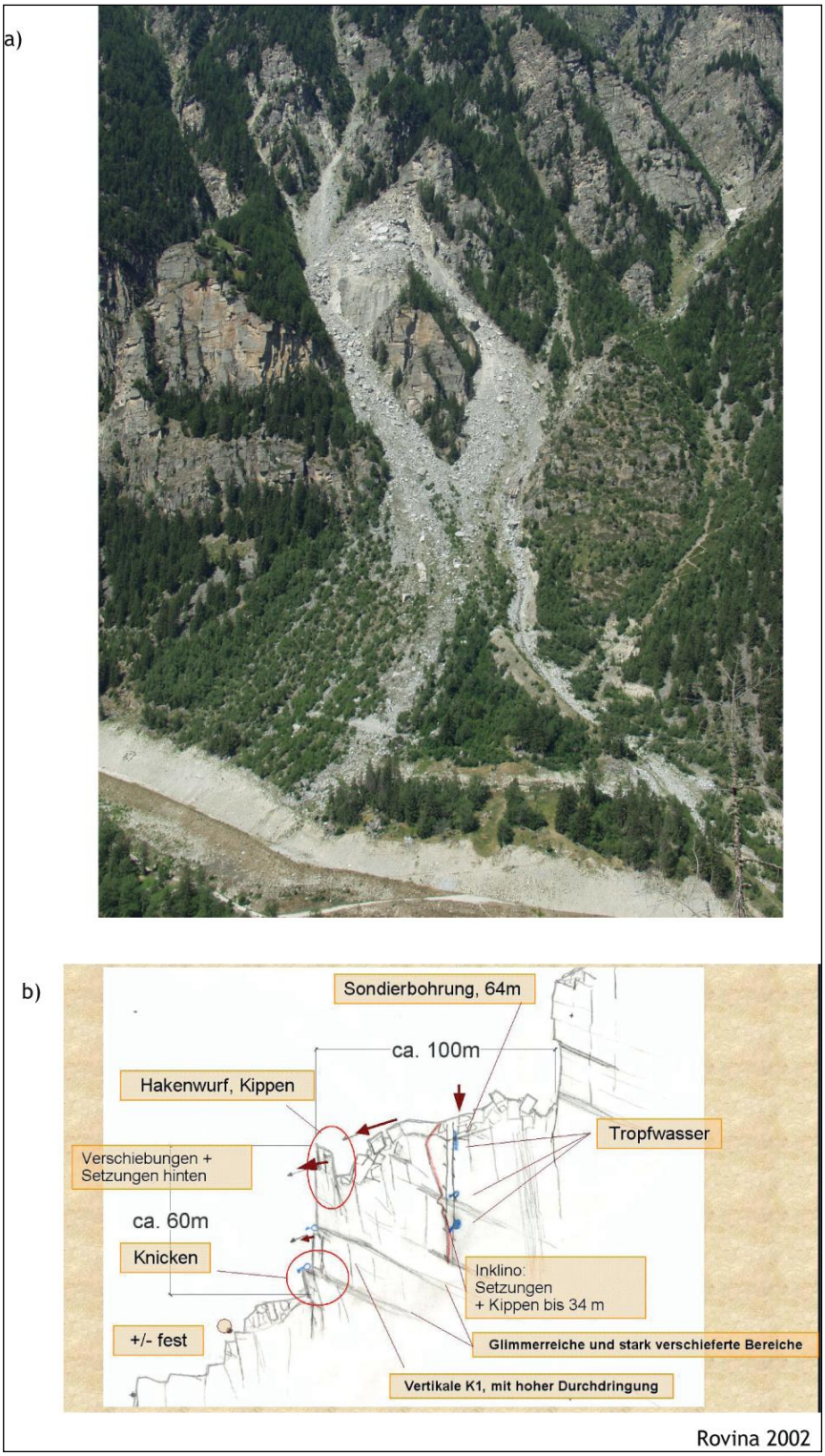

Figure 2.3. 2002 rockslide of Medji. a) Overview of the current situation b) Schematic cross section of the situation before the 2002 failure (From Rovina, 2002).

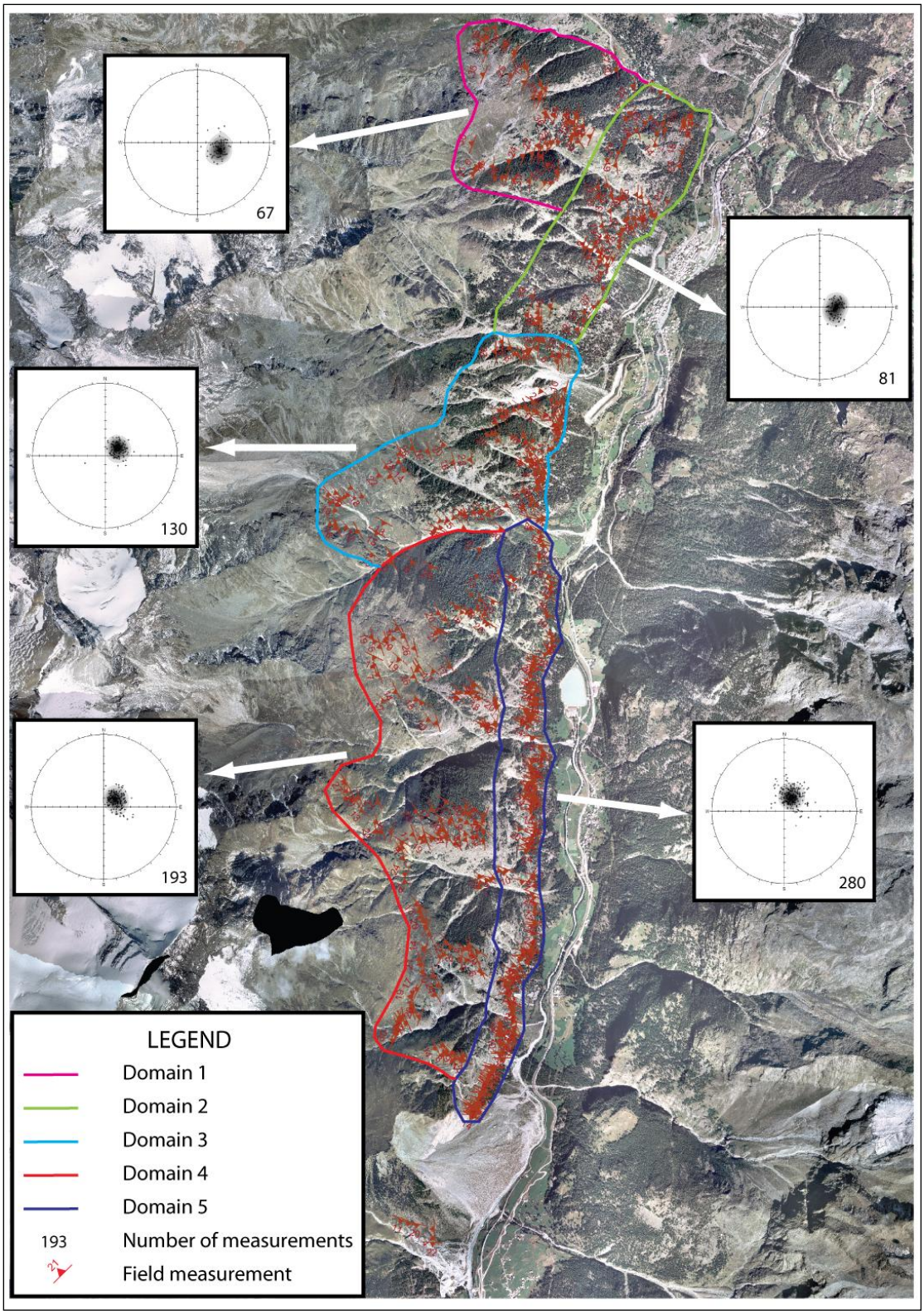

Figure 2.4. Foliation orientation and domains from field measurements.

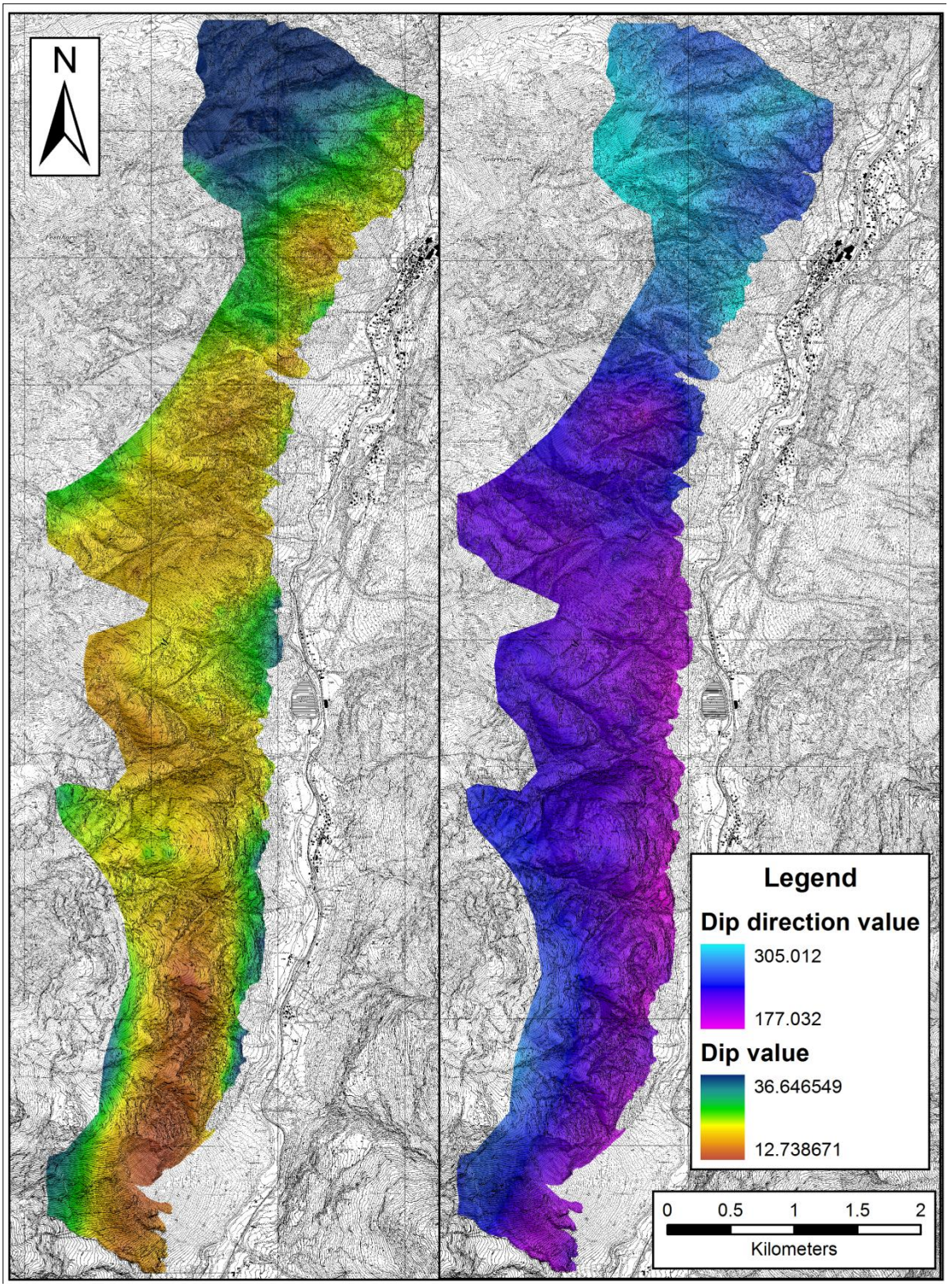

Figure 2.5. Continuous grid surfaces representing spatial variation of dip (left) and dip direction (right) of foliation. Grids were built using disjunctive kriging.

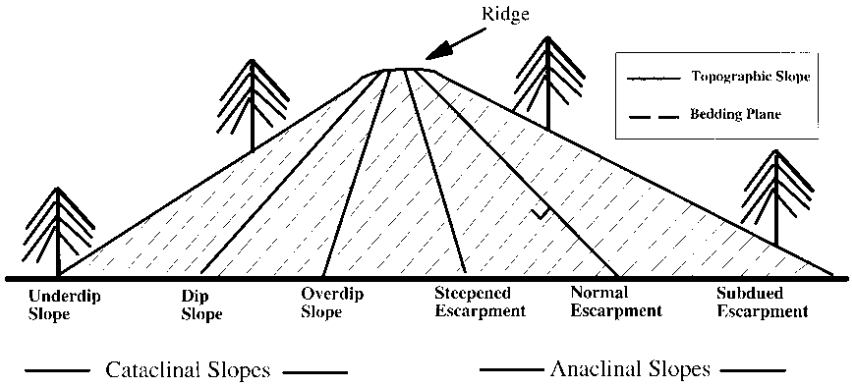

Figure 2.6. Schematic representation of the relationships between topography and penetrative discontinuities (from Meentemeyer and Moody, 2000). Orthoclinal slopes are not shown.

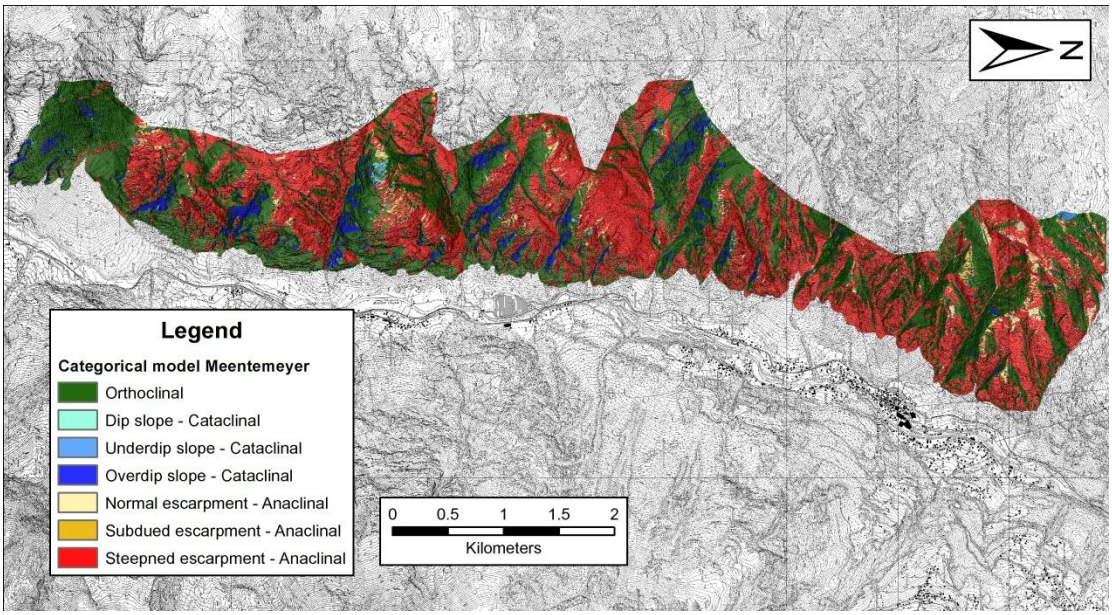

Figure 2.7. Slope classification for the study area using the TOBIA categorical model.

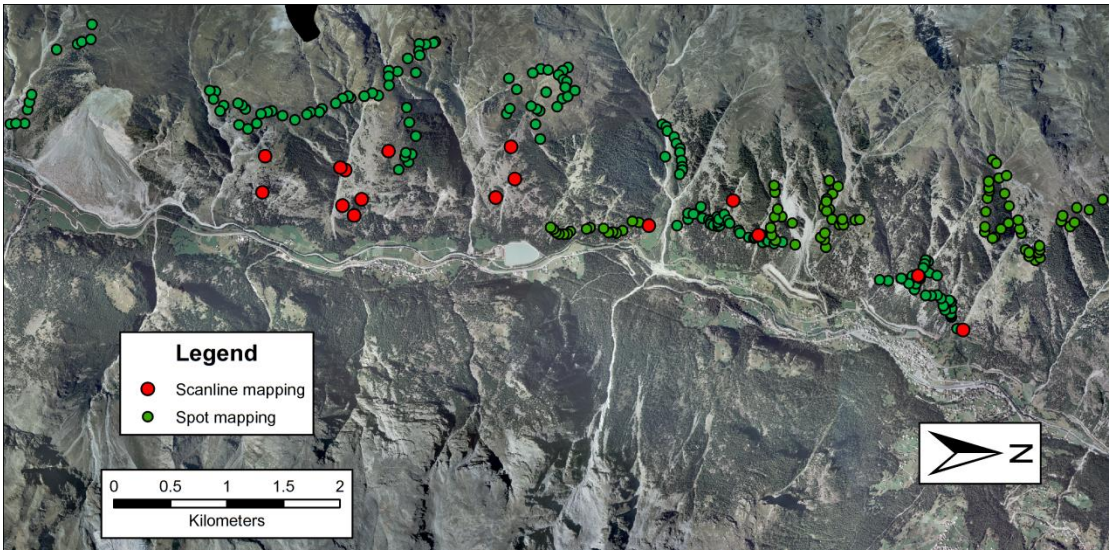

Figure 2.8. Spatial distribution of the sampled locations within the study area.

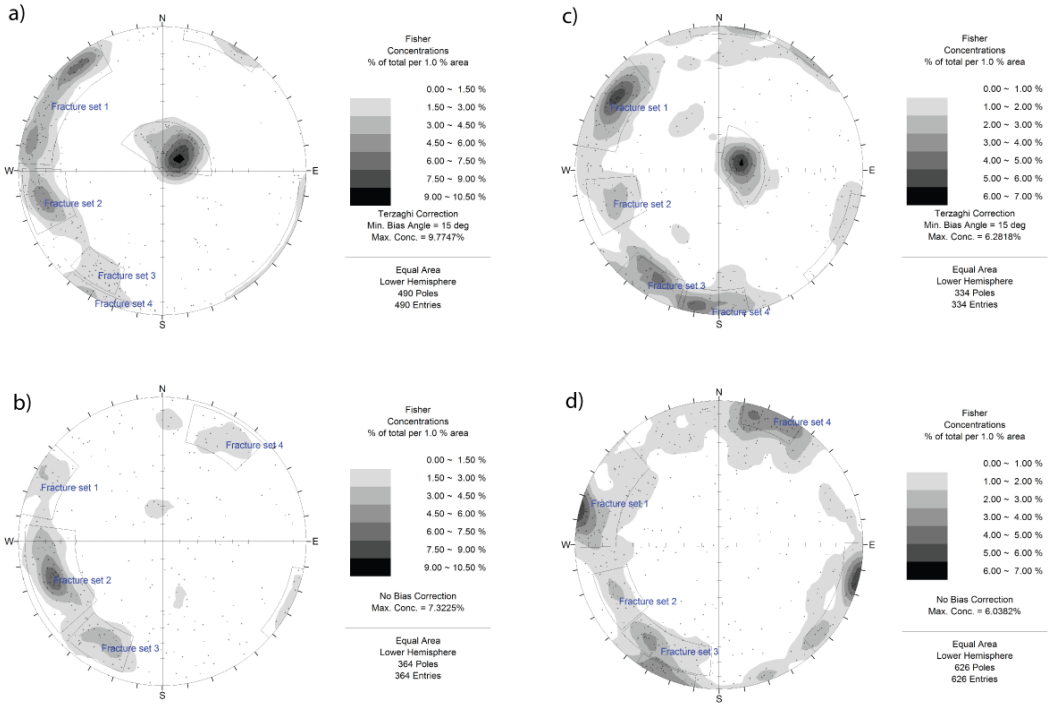

Figure 2.9. Stereoplots of meso-scale discontinuities from field recognition for the study area (equal area, lower hemisphere). a) Results from scanlines southern domain (Zueger, 2007); b) Results from spot mapping southern domain; c) Results from scanlines northern domain; d) Results from spot mapping northern domain

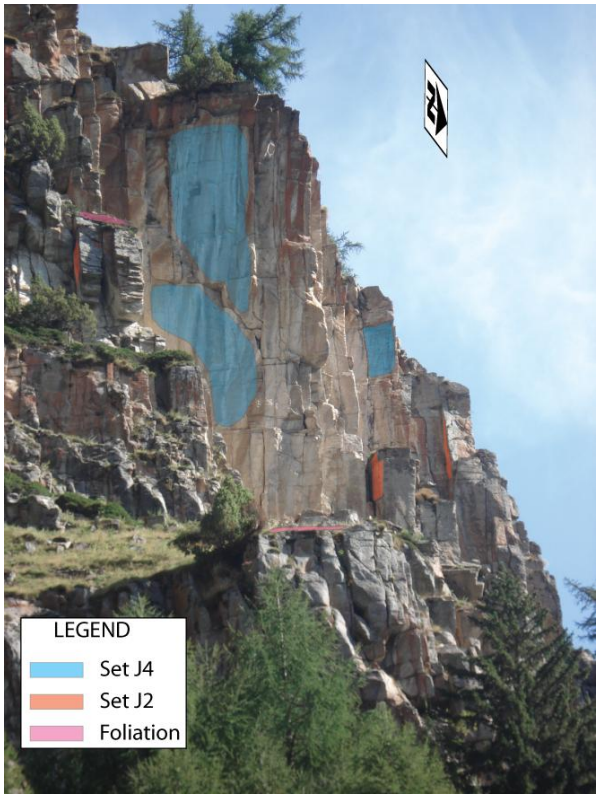

Figure 2.10. Picture showing the influence of meso-scale fracture sets on the construction of landscape. In the example, three sets control slope walls.

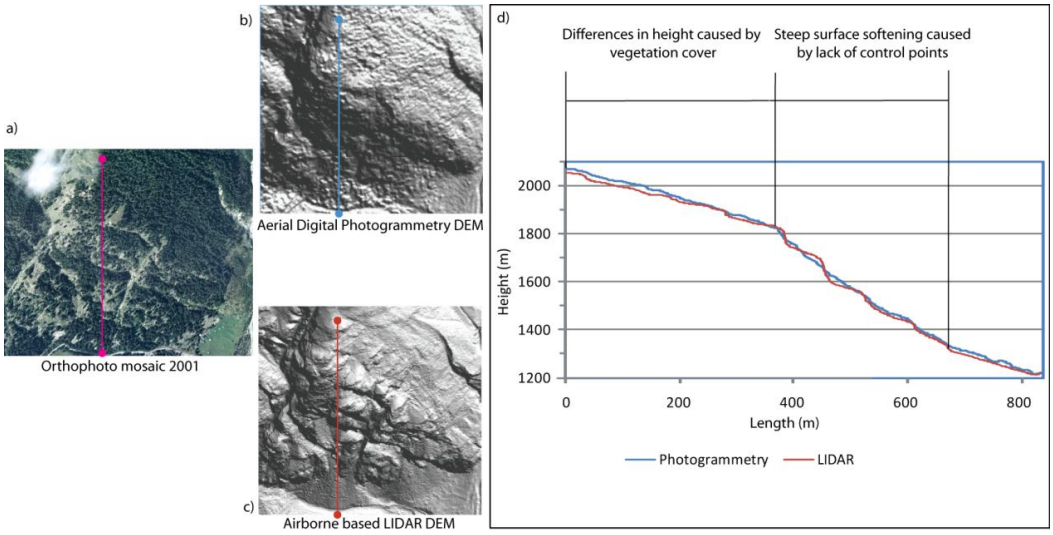

Figure 2.11. Changes observed on DEMs for the Matter Valley. a) View of orthophoto from the area. b) Photogrammetry DEM, c) LIDAR DEM, d) Comparison of profiles extracted from the DEMs (different scale for height and length).

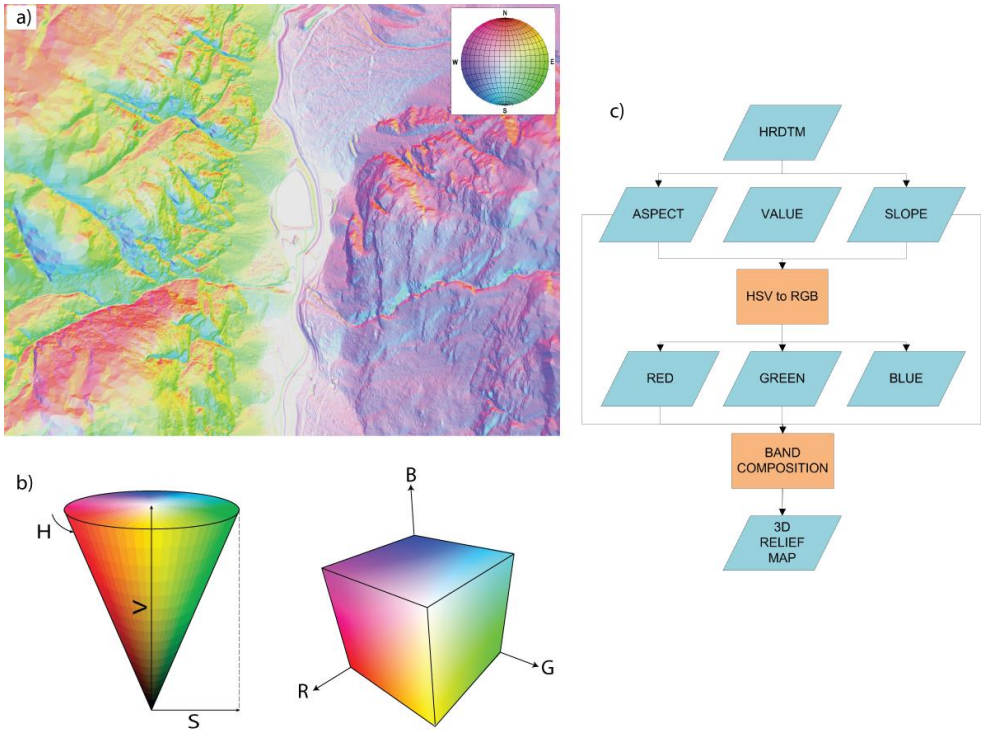

Figure 2.12. Construction of a 3D shaded relief map. a) Example of 3D shaded relief map for the area of the Matter Valley, b) differences in representation between HSV and RGB color model schemes, c) Flowchart of construction using ArcGIS.

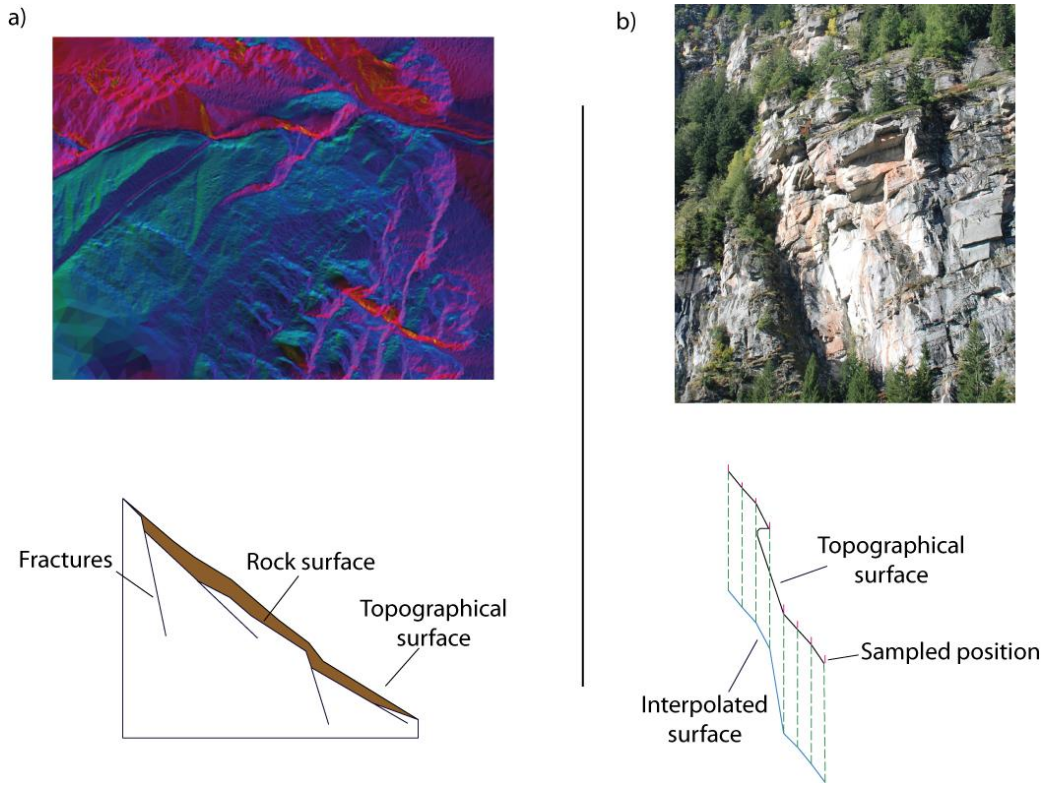

Figure 2.13. Principal source of errors a) Thick soil covers, b) Overhanging blocks on walls.

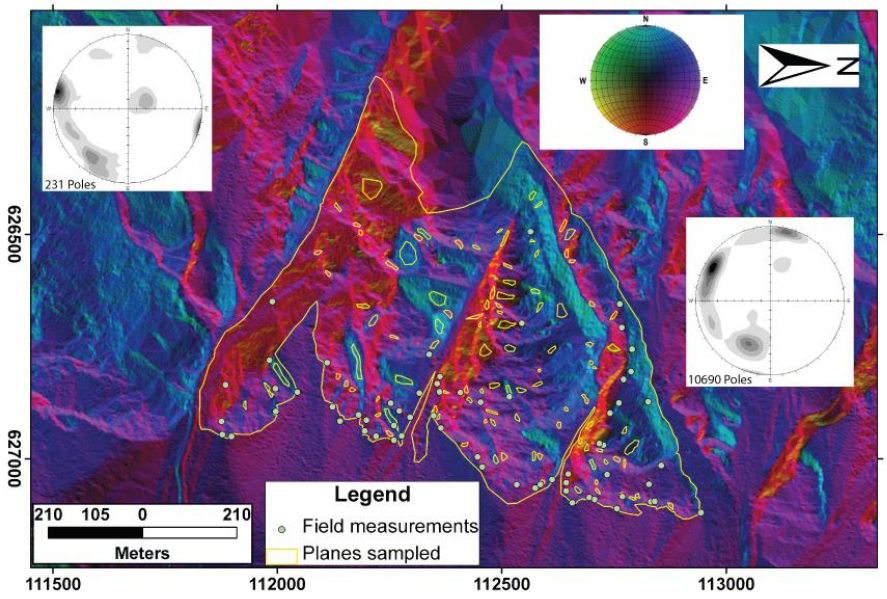

Figure 2.14. An example of a 3D shaded relief map showing fracture orientations in the Northern part of the study area (Walkerschmatt). Color scheme has been inverted to help visualization. The stereoplot from DEM analysis to the right, and the stereoplot from field mapping to the left are shown (equal area, lower hemisphere projection). Smaller polygons represent areas selected for DEM analysis and the large polygon corresponds to limits of the sub-domain. Green dots represent field stations.

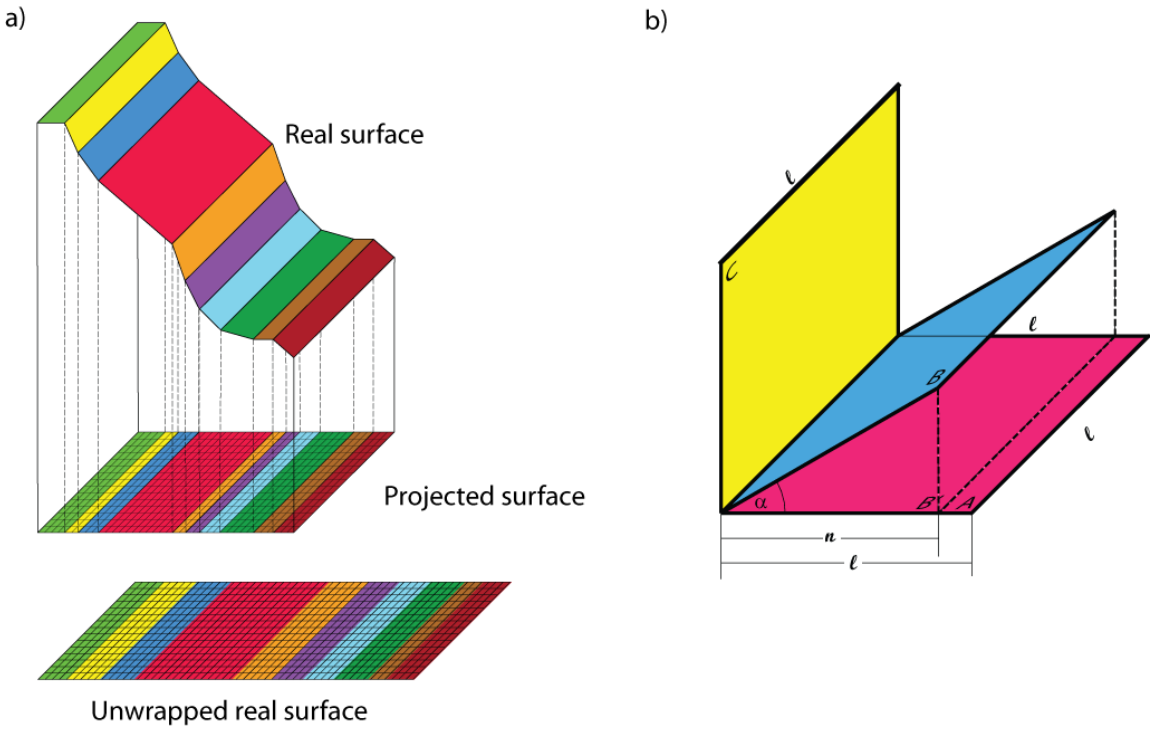

Figure 2.15. Areal correction for data extracted from a 3D color shaded relief map. a) Schematic representation showing the bias produced by slope angle between a projected surface and the real surface, b) Geometrical relationships between planes with similar area but different inclination angle.

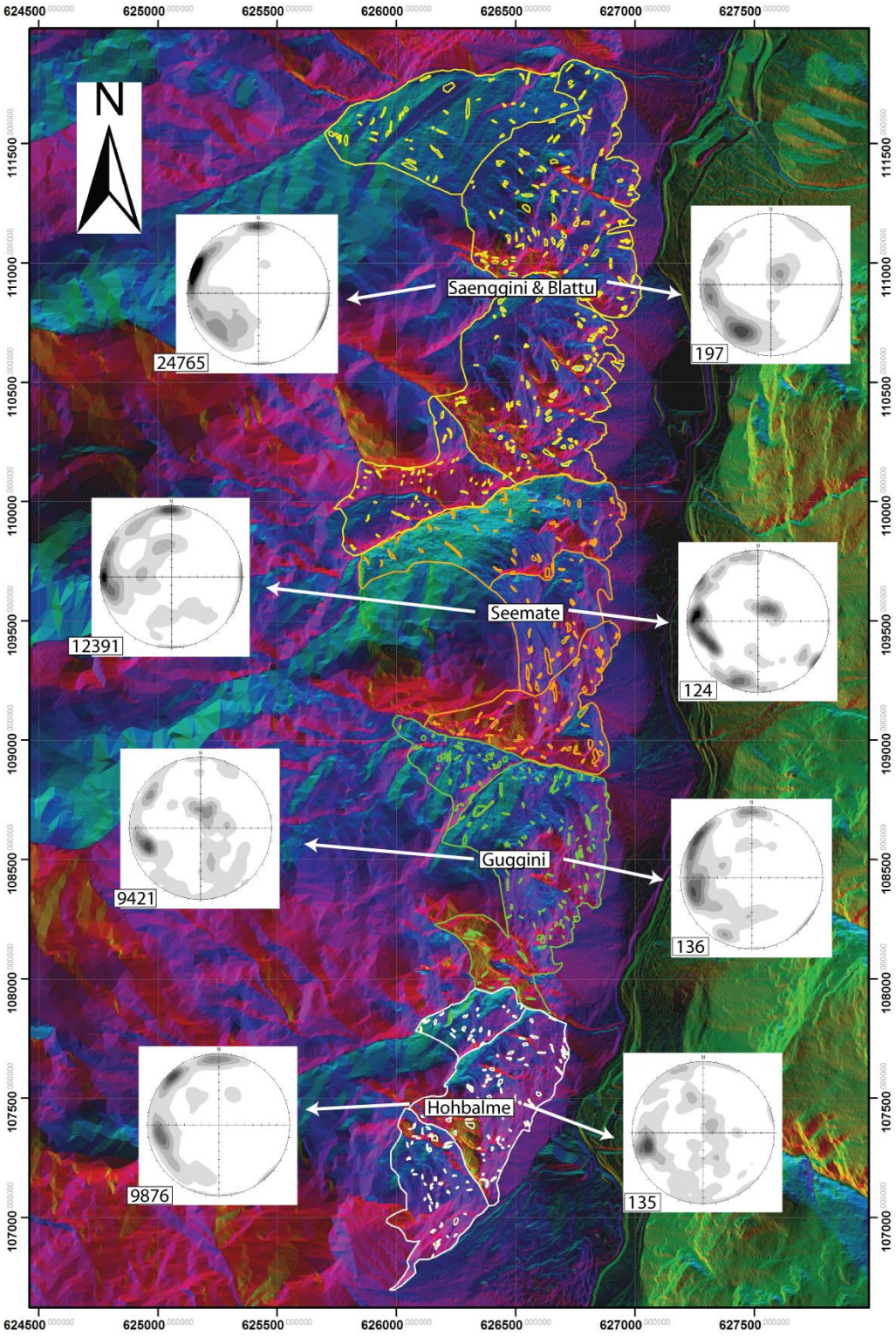

Figure 2.16a. 3D shaded relief with stereoplots of meso-scale discontinuities to the South of the Blattbach River. Stereoplots obtained by DEM-based analysis to the left and by field recognition to the right. Large polygons represent limits of the sub-domains. Small polygons are sampled areas. Color of polygons is different for each sub-domain.

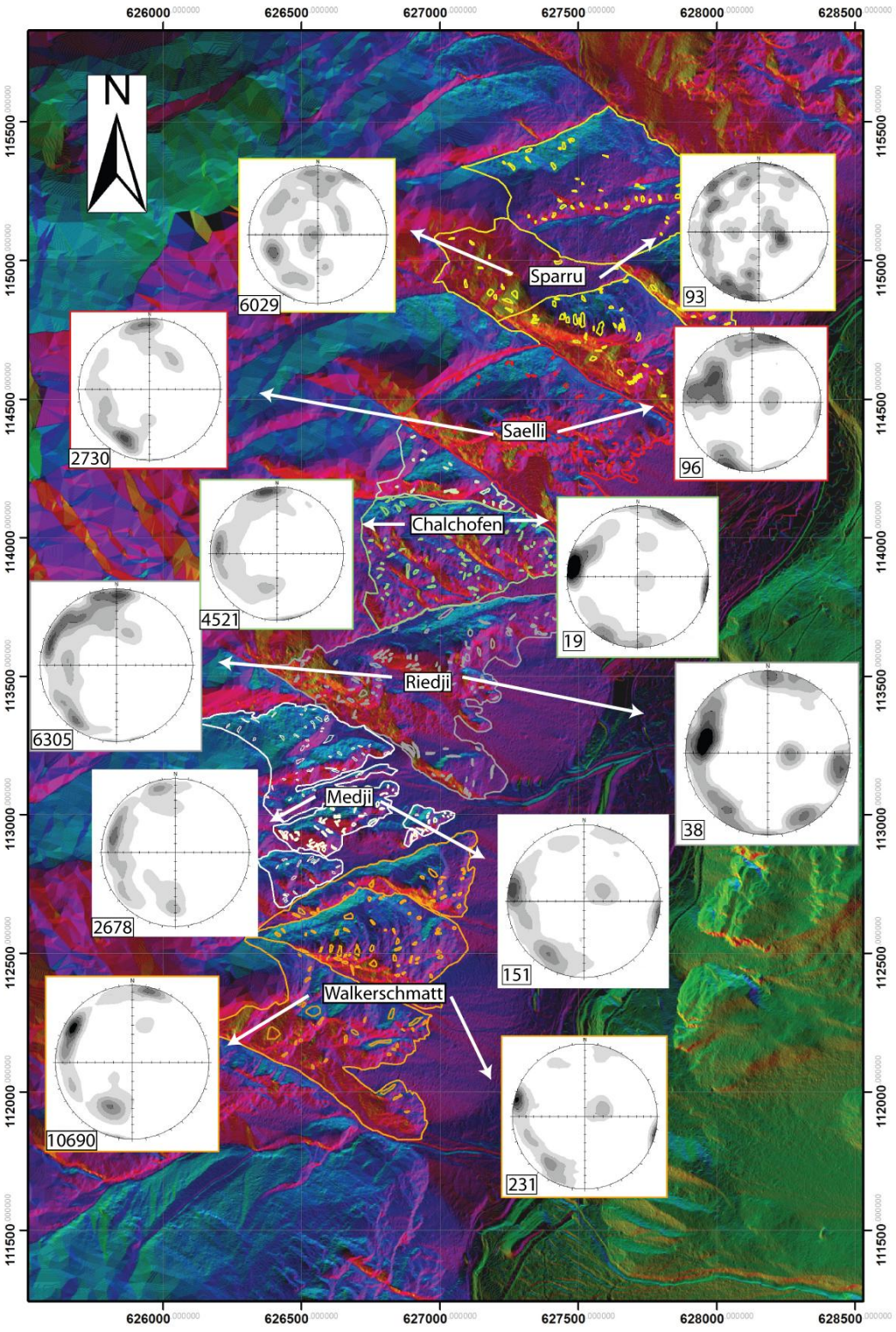

Figure 2.16b. 3D shaded relief with stereoplots of meso-scale discontinuities to the North of the Blattbach River. Stereoplots obtained by DEM-based analysis to the left and by field recognition to the right. Large polygons represent limits of the sub-domains. Small polygons are sampled areas. Color of polygons is different for each sub-domain.

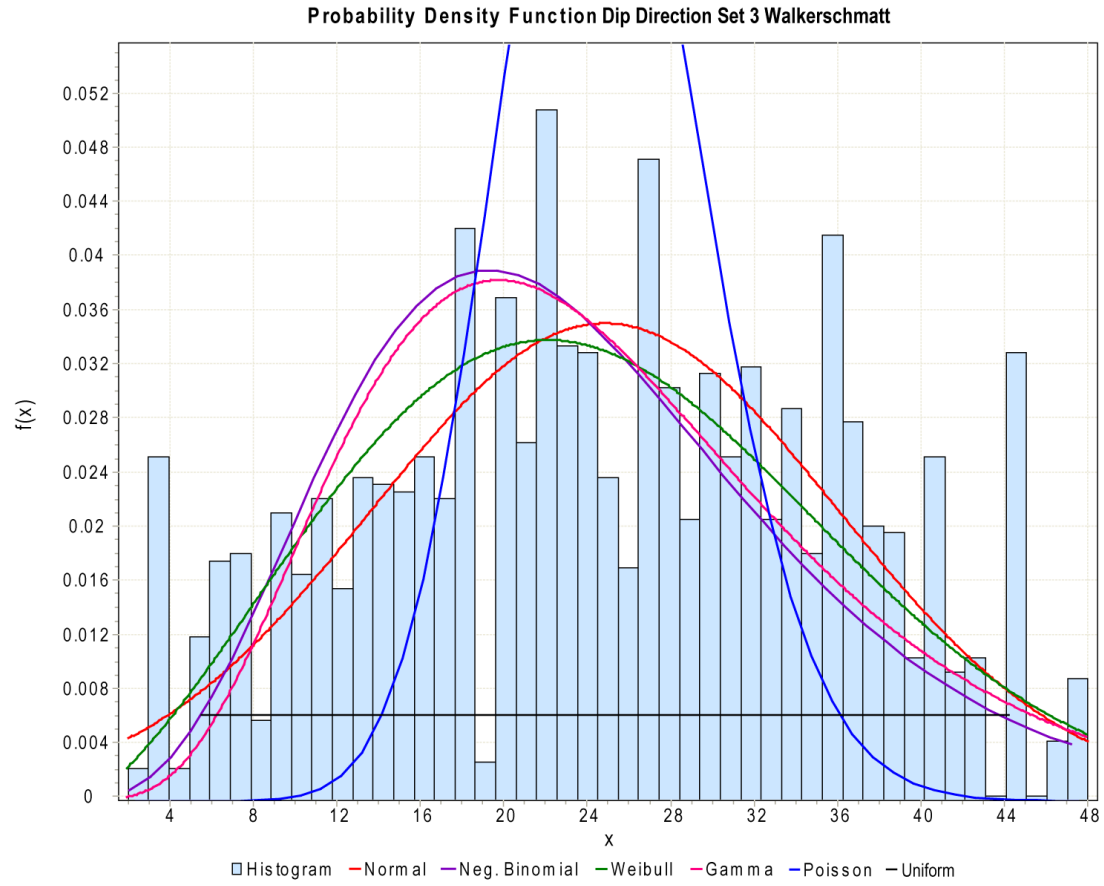

Figure 2.17. Probability density function for dip direction of set 3 in the area of Walkerschmatt. Histogram represents the data obtained by DEM-based analysis. Lines represent five of the most representative fitted distributions for the sample.

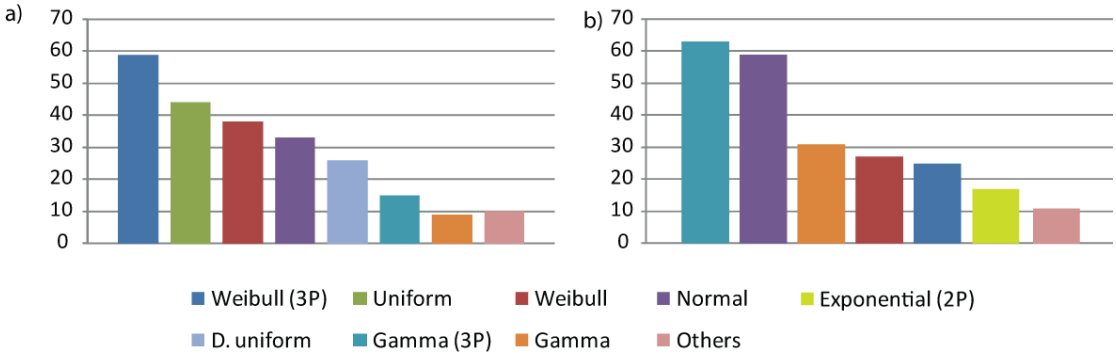

Figure 2.18. Ranking of distributions using a) Kolgomorov-Smirnov test and b) Anderson-Darling test. The number on the y-axes represents the number of times a distribution was scored at the top three for all 78 samples.

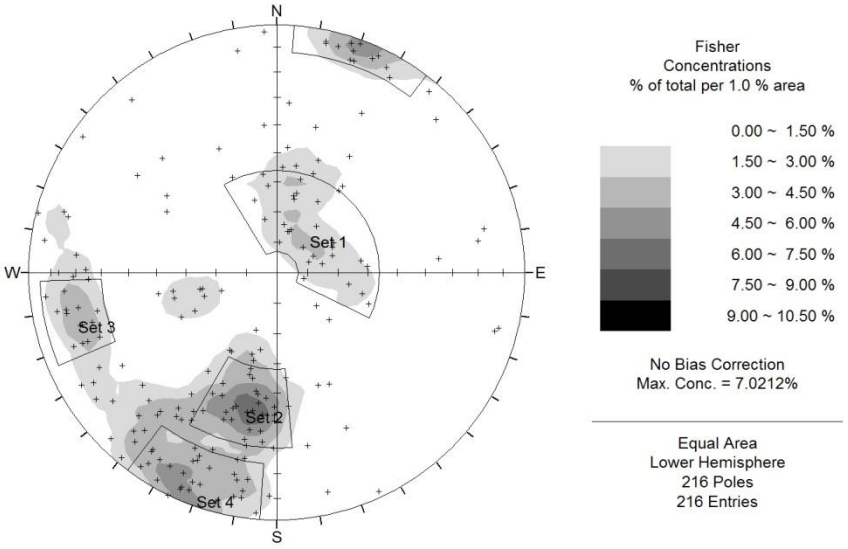

Figure 2.19. Stereoplot showing large scale discontinuity orientations from field observation. Four main sets were found and described.

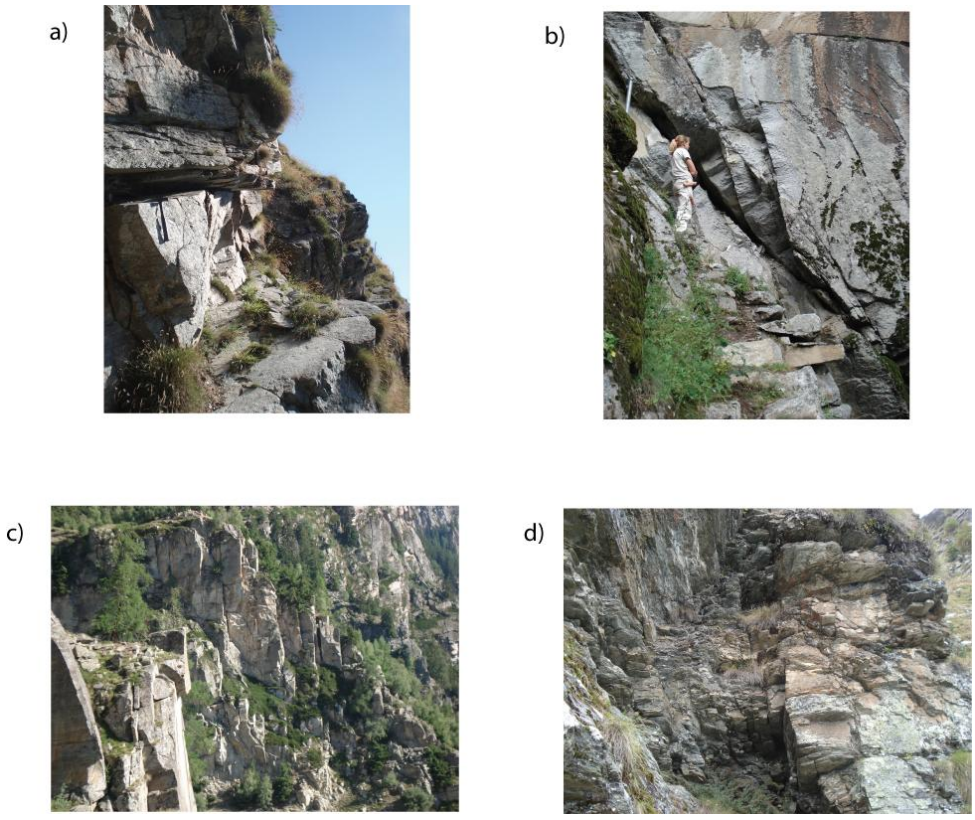

Figure 2.20. Fault Examples of large scale fracture sets. a) Ductile shear zone reactivated by brittle fractures in the area of Guggini (F1), b) fault with gouge and secondary structures (Riedels) lower part of Walkerschmatt (F2), c) fracture and fracture zones parallel to the valley axis (F3) and d) fracture zone in the area of the Guggigraben between Guggini and Seemate (F4).

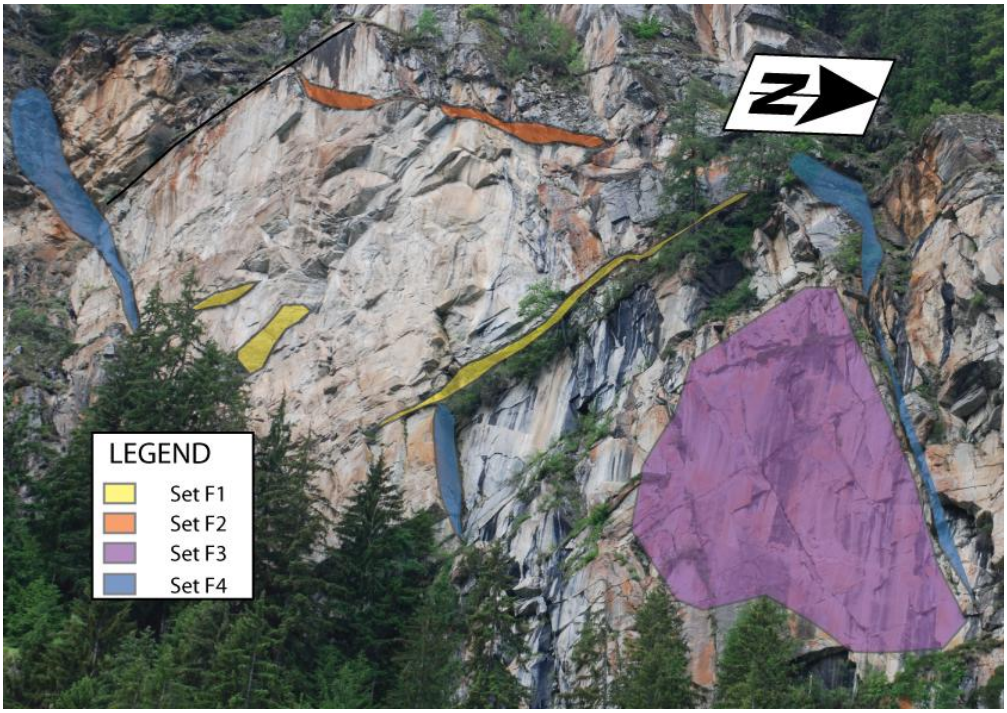

Figure 2.21. Photograph taken in the area of Saenggini close to the Blattbach River showing the four main large scale fracture sets for the study area.

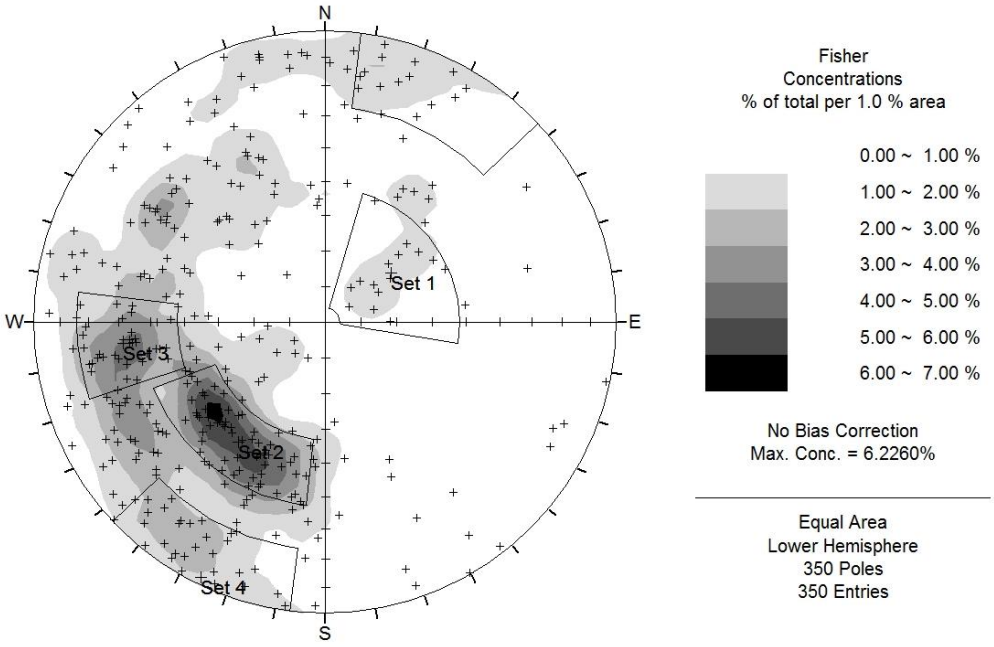

Figure 2.22. Stereoplot showing orientation for the lineaments identified from DEM analysis and photo-interpretation (stereonet equal area, lower hemisphere).

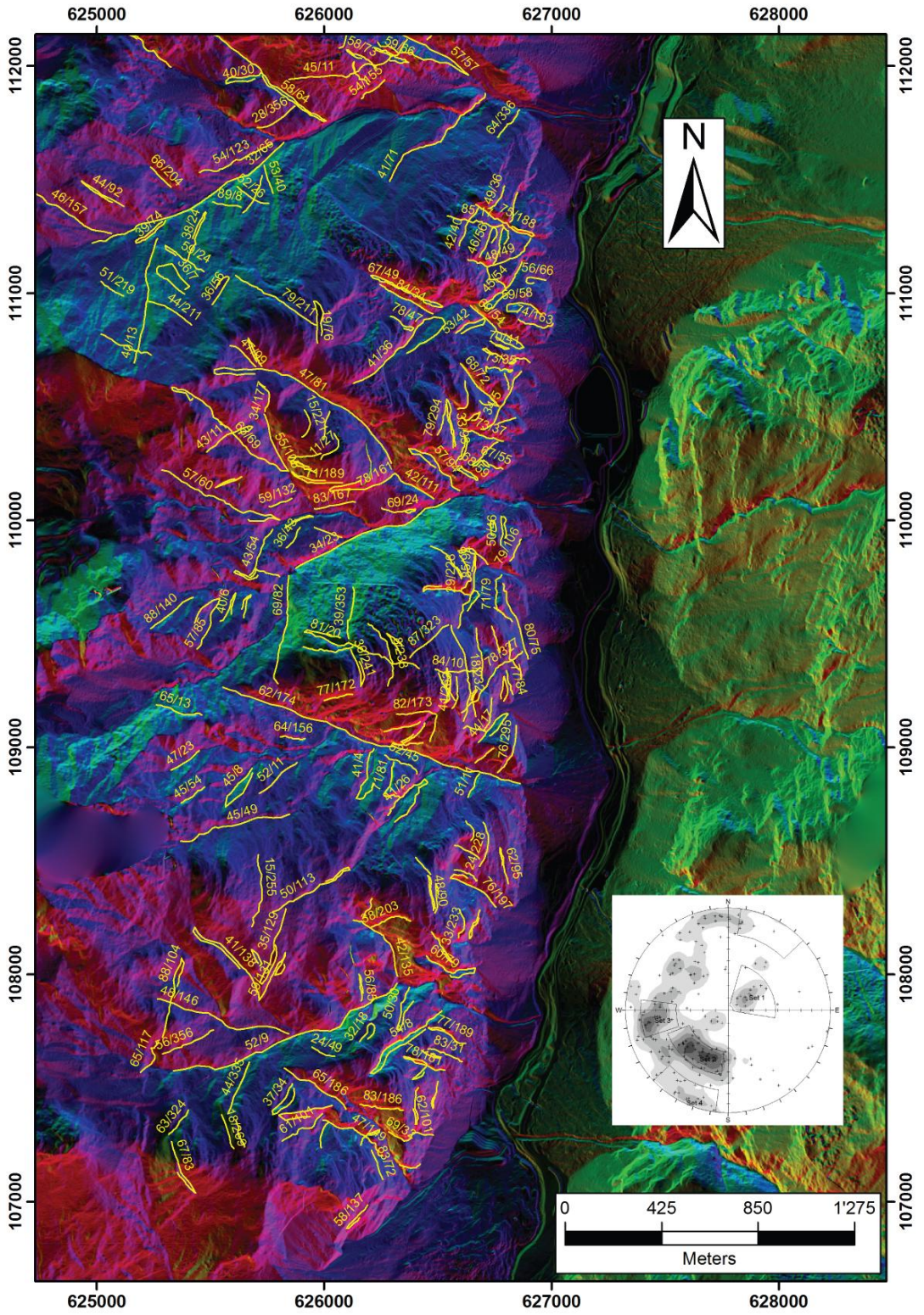

Figure 2.23a. Map of lineaments and their calculated orientations for the area to the S of the Blattbach River.

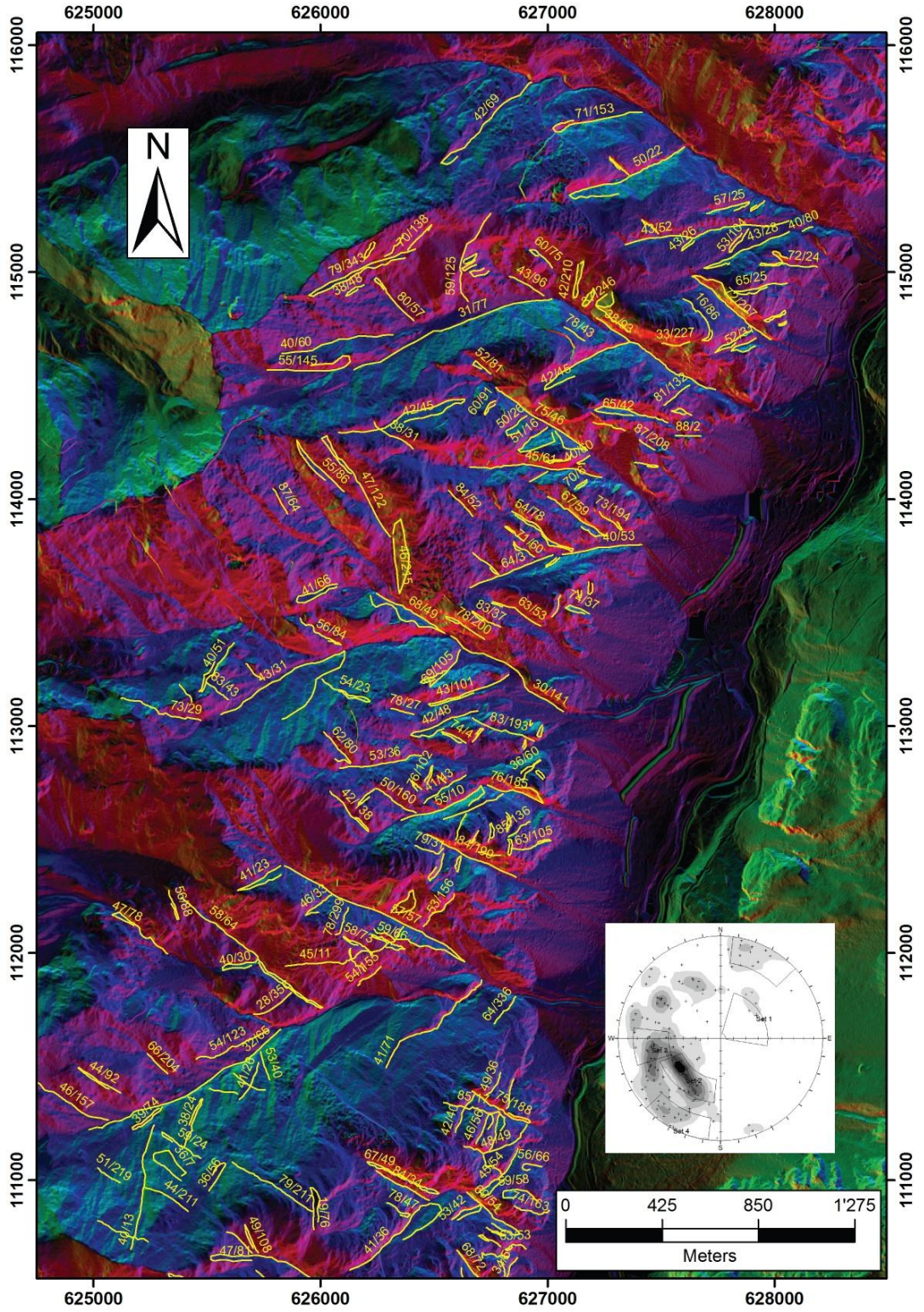

Figure 2.23b. Map of lineaments and their calculated orientations for the area to the N of the Blattbach River.